
Topological carbon materials: a new perspective

Yuanping Chen¹, Yuee Xie¹, Xiaohong Yan¹, Marvin L. Cohen², Shengbai Zhang³

¹ Faculty of Science, Jiangsu University, Zhenjiang, 212013, Jiangsu, China

² Department of Physics, University of California at Berkeley, and Materials Sciences Division, Lawrence Berkeley National Laboratory, Berkeley, California, 94720, USA.

³ Department of Physics, Applied Physics, and Astronomy Rensselaer Polytechnic Institute, Troy, New York, 12180, USA.

Outline:

I. Introduction	1
II. Carbon structures: from one to three dimensionalities.....	2
2.1 One dimension: polyacetylene	2
2.2 Two dimension: graphene, graphyne and Kagome graphene	3
2.3 Three dimension: graphene networks and carbon foams.....	6
III. Topological phases in general	9
3.1 Nodal points: Weyl point, Triple point, Dirac point.....	10
3.2 Nodal lines: Nodal ring, Nodal chain/link, Hopf link/chain.....	12
3.3 Nodal surfaces: planer surface, sphere surface.....	13
IV. Topological properties of carbon.....	14
4.1 Orbital physics in graphene-based structure	14
4.2 Topological properties of graphene nanoribbons junctions.....	16
4.3 Dirac points in two-dimensional carbon sheets.....	17
4.4 Topological properties of three-dimensional carbon allotropes.....	18
4.5 Extension to boron and beyond.....	31
V. Final remarks.....	32

I. Introduction

Carbon, being one of the most abundant elements, has numerous one-dimensional (1D), two-dimensional (2D), and three-dimensional (3D) allotropic structures¹⁻³. Although, graphite and diamond are the best known and studied carbon forms, in the past several decades, three other carbon forms, fullerenes⁴, carbon nanotubes⁵ and graphene⁶, have become the focus of extensive research. Studies of these three carbon forms, have had a large impact on both scientific and industrial communities, and the search for new structures and applications continues⁷⁻⁹

Many important and unique properties of carbon can be attributed to its position in the Periodic Table. Each carbon atom has four valence electrons with an atomic configuration $2s^2 2p^2$. These four valence electrons can in principle be engaged in sp , sp^2 and sp^3 hybridizations to form a variety of allotropes or compounds with different bonding configurations¹⁰. For example, carbon can form triple bonds in the sp hybridization in graphyne, double bonds in the sp^2 hybridization in graphene, and single bonds in the sp^3 hybridization in diamond. Because of this rich hybridization capacity, the associated new structures, and the high potential for applications, the study of carbon materials has been a major focus of material science and condensed matter physics¹¹⁻¹³

In the last decade, an active topic has emerged focusing on the topological behavior of electronic states¹⁴⁻¹⁸. Although many different phases of matter can be described well by the Landau symmetry-breaking theory where phase transitions can be traced back to changes in the order parameters going from one phase to another, phase transitions can occur without the breaking of symmetry for the phase. Many of these can be classified as topological phase transitions. A well-studied example is the topological insulator^{19,20}, in which the bulk solid is insulating while an edge (or surface) is conducting. Another class of materials of current interest is those featured by low-energy excitations with counterparts in high-energy physics, such as the low-energy excitations in Dirac (Weyl) semimetals²¹⁻²³ which behave just like the Dirac (Weyl) fermions. Since Lorentz symmetry is not guaranteed in condensed matter, there can be more types of fermions without counterparts in high-energy physics, and these new fermions bring new understanding to condensed matter physics^{24,25}

At present, the study of topological physics in condensed matter mainly involves materials made of heavy elements that maximize the spin orbit coupling (SOC)²⁶⁻³⁰, as a large SOC is often a prerequisite for experimentally measurable topological properties. Carbon is a counter-example. In fact, the first theoretically predicted topological insulator (TI) is graphene³¹. However, research has since drifted away from carbon because the SOC in carbon is exceedingly small. It is well known that graphene is a Dirac semimetal^{32,33}, its lowest excitation is a Dirac fermion. Because of the small SOC, on the other hand, one may treat the spin degree of freedom of graphene as a dummy variable. Interestingly, under such an approximation, graphene can be classified as a Weyl semimetal, whose topological classification is fundamentally different from any of the SOC-based classifications^{34,35}. Previous studies have identified different classes of topological semimetallic carbon allotropes with Weyl points³⁶⁻⁴¹, nodal loops⁴²⁻⁴⁹, and Weyl surfaces^{50,51}

In this review, we first give a brief summary of the development of carbon allotropes from 1D to 3D. Next, we will discuss topological properties of carbon materials and their physical origin. Then, we will consider possible expansion of the topological study of carbon materials to other light-element materials such as boron. Finally, we will present future prospects in pursue of topological physics within carbon allotropes.

II. Carbon structures: from one to three dimensions

In recent decades, with the development of nanotechnology, C₆₀ fullerenes, carbon nanotubes, and graphene have been synthesized and have become one of the best-studied group of nanostructures⁴⁻⁶. Recently, 3D graphene networks have been proposed, and some of them, such as the carbon honeycomb⁵², have been experimentally realized. With the rapid progress of science and technology in this area, it can be expected that more novel carbon materials will be realized in the foreseeable future. In the following, we will introduce typical carbon allotropes from one to three dimensions.

2.1 One dimension: polyacetylene

Polyacetylene: Based on a single-atom carbon chain, polyacetylene is one of the simplest 1D carbon systems⁵³. Many 1D, 2D, and 3D carbon allotropes can be constructed by connecting

polyacetylene⁵⁴⁻⁵⁶, such as carbon nanotubes, graphene and 3D graphene networks.

Polyacetylene usually refers to an organic polymer with the repeating unit $(C_2H_2)_n$, as shown in Fig. 1. It is a long chain of carbon atoms with alternating single and double bonds between them and each carbon atom has one attached hydrogen atom. Polyacetylene may also be viewed as a polymerization of the acetylene molecules to yield a chain of repeating olefin groups. It is conceptually important, as the discovery of polyacetylene and its high conductivity upon doping helped the establishment of the field of organic conductive polymers⁵⁷. The high electrical conductivity of polymers led to the use of organic compounds in microelectronics, which was recognized by the Nobel Prize in Chemistry in 2000⁵⁸.

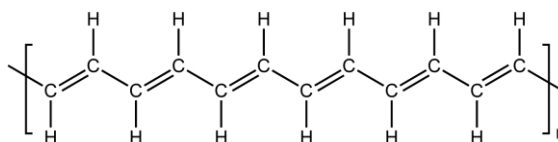


Figure 1. Atomic structure of polyacetylene.

Besides polyacetylene, there are other 1D carbon structures such as carbon threads⁵⁹, carbon nanowires⁶⁰, graphene nanoribbons, and carbon nanotubes. The last two will be discussed later.

2.2 Two dimensions: graphene, graphyne and Kagome graphene

Graphene: Graphene is a 2D single-layer honeycomb nanosheet⁶¹, as shown in Fig. 2(a). There is no doubt that it is one of the most important nanomaterials studied in the last several decades⁶²⁻⁶⁶. Graphene receives tremendous attention not only because it is one of the first 2D nanomaterials, but also because it possesses numerous astonishing physical and chemical properties, such as an ultrahigh electron mobility⁶⁷, a high mechanical strength⁶⁸, and a high thermal conductivity⁶⁹.

The first method used to obtain graphene is mechanical exfoliation with scotch tape⁷⁰. The exfoliated graphene is of very high quality, but the above method is neither high-throughput nor high-yield. There have been numerous proposals to produce high-quality graphene with more efficient and scalable approaches⁷¹⁻⁷⁴. Alternatives to the mechanical exfoliation may be classified into three categories: (i) chemical vapor deposition (CVD), such as the decomposition of ethylene on nickel surfaces⁷⁵, (ii) bottom-up methods to grow graphene directly from an organic precursor⁷⁶, and (iii)

epitaxial growth on electrically insulating substrate such as SiC⁷⁷. A thorough discussion of the various fabrication methods for graphene can be found elsewhere⁷⁸⁻⁸⁰.

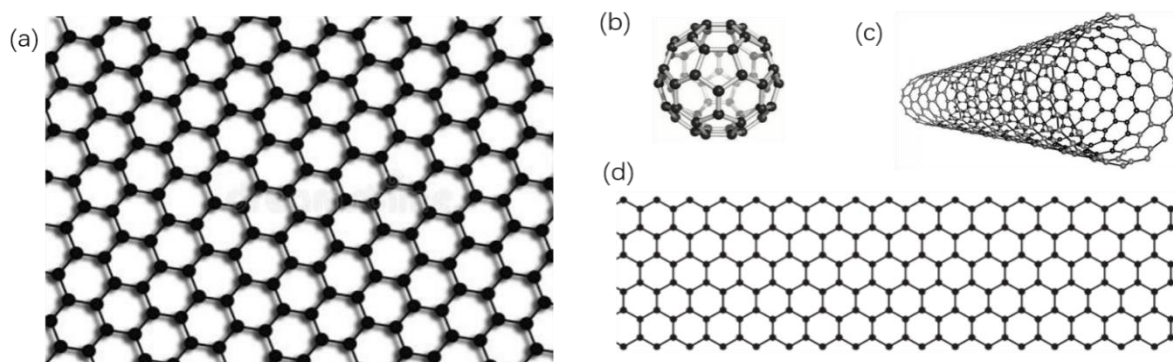


Figure 2. Graphene can be used to construct other carbon materials. (a) 2D graphene, (b) 0D fullerene, (c) carbon nanotube, (d) graphene nanoribbon.

The uniqueness of graphene in the family of carbon allotropes is that it may be viewed as the parent material from which many other carbon structures can be constructed⁸¹⁻⁸⁶. For example, it can be stacked to produce 3D graphite, rolled into a 1D carbon nanotubes [Fig. 2(b)], or wrapped to construct a 0D fullerenes [Fig. 2(c)]. Moreover, graphene can be tailored and lithographed into desired patterns^{87,88}.

By cutting graphene along certain directions, **1D graphene nanoribbons (GNRs)** with different edges are obtained, such as armchair-edged and zigzag-edged nanoribbons⁸⁹⁻⁹². Figures 2(d) shows a zigzag-edged nanoribbon. Numerous approaches have been reported to produce GNRs with various chemophysical properties⁹³⁻⁹⁶. The 1D carbon nanotube in Fig. 2(c) is simply a roll up of a graphene nanoribbon.

Graphyne: Graphyne is one-atom-thick planar sheets of sp and sp^2 -bonded carbon atoms arranged in a crystal lattice⁹⁷. The proposed structures of graphyne are constructed by inserting acetylene bonds in places of C-C polyacetylene single-bonds in a graphene lattice⁹⁸, see for example, the three types of graphyne in Fig. 3. There is a variety of possibilities due to the multiple arrangements of sp and sp^2 hybridized carbon atoms^{41,99,100}. In addition, graphyne can be arranged either in a hexagonal or a rectangular lattice^{101,102}. It has been shown theoretically that graphynes possess direction-dependent Dirac cones^{98,103}. Among the graphynes with a rectangular lattice, the 6,6,12-graphyne may hold the most potential for applications^{104,105}. To date, synthesized graphyne samples

have shown to have a melting point of 250-300 °C¹⁰⁶ and a low reactivity in decomposition reactions with oxygen, heat, and light¹⁰⁷⁻¹¹⁰.

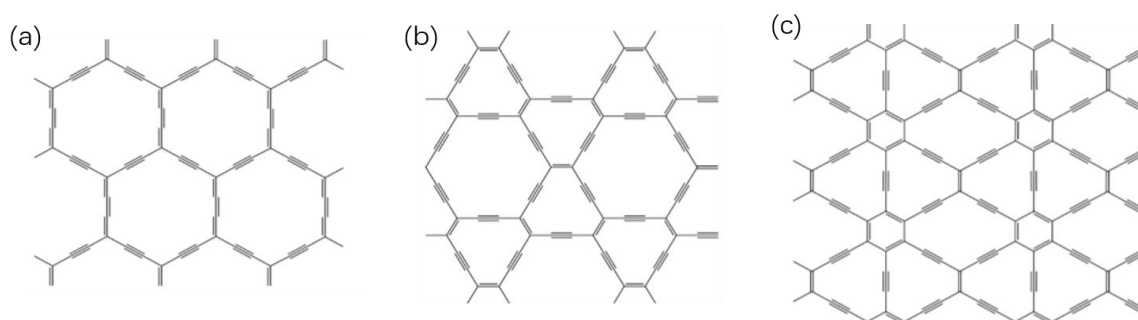


Figure 3. Three types of graphynes, (a) α -graphyne, (b) β -graphyne, and (c) 6,6,12-graphyne.

Kagome graphene¹¹¹: Kagome graphene is a monolayer carbon sheet as shown in Fig. 4(a). It has twice as many atoms as a regular Kagome lattice. Should the bond length between two adjacent different-colored atoms “shrinks” to zero, one recovers the regular Kagome lattice. By inserting acetylenic dimers between the neighboring triangles, a family of Kagome-like structures can be generated. For example, a Kagome graphyne containing one dimer between triangles is shown in Fig. 4(b).

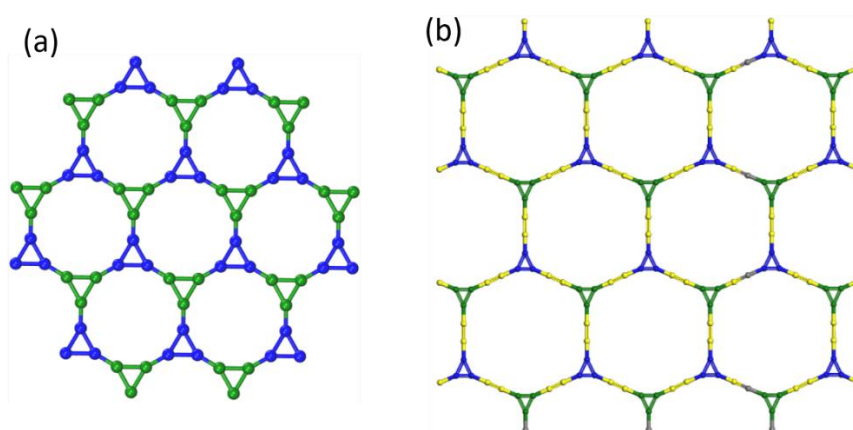


Figure 4. (a) Kagome graphene and (b) Kagome graphyne.

The lattice constant of the Kagome graphene is 5.19 Å. The bond length within a carbon triangle is 1.42 Å, while between the triangles is 1.35 Å. The former is very close to that of graphene, while the latter is between graphene and acetylene. Although the Kagome graphene contains carbon triangles,

its calculated cohesive energy of 8.26 eV/atom is less than either α - or β -graphynes, 8.28 and 8.35 eV per carbon atom, respectively. Theoretical calculations indicate that the Kagome graphene and graphyne are all stable¹¹¹. Although Kagome graphene has not been synthesized, a possible route for its experimental realization is proposed¹¹¹. The elemental building unit of the triangular carbon rings of Kagome graphene already exists in laboratory as various cyclopropane molecules. One may thus tailor the ligand chemistry of the cyclopropanes to realize a self-assembly of the Kagome graphene. In terms of the choice of the substrate, the self-assembly process may be carried out on single-layer boron nitride sheet¹¹¹.

Beside graphene, graphyne and Kagome graphene, other 2D carbon structures have also been proposed¹¹²⁻¹¹⁶, such as T-graphene¹¹⁶.

2.3 Three dimension: graphene networks and carbon foams

Early carbon materials known to us are 3D allotropes, such as naturally occurring graphite and diamond^{117,118}. While graphite is a 3D stacked graphene monolayer bound by van der Waals interactions, diamond can also be viewed as an interlocked stacking of graphene layers with buckling due to sp^3 bonding between carbon atoms. These bonds result in the hardest material found thus far in nature¹¹⁹.

However, graphite and diamond are not the only possibilities. Many more 3D carbon materials can be built out of graphene in a similar fashion¹²⁰⁻¹²⁸. For example, Fig. 5(a) shows a structure formed by interpenetrating graphene layers¹²⁹. When viewed from the top, the 3D network looks like a Kagome lattice, so it is named the carbon Kagome lattice (CKL). Its relation with the Kagome lattice is shown in Fig. 5(b). If one envisions that each infinitely long zigzag carbon chain in a CKL is collapsed to a 2D lattice point, then the two structures become identical. Although the structure consists of triangular rings (as can be seen from a top view), the CKL exhibits an exceptional stability similar to C_{60} . The reason is because the CKL is made of graphene sheets (as can be seen from a side view). A related structure is the interpenetrated graphene networks (IGN) in Fig. 5(c)³⁶, which is also made of two sets of interlocked graphene sheets [see Fig. 5(d)]. One obtains the CKL from IGN by applying a compressive stress along the direction indicated by the arrows in Fig. 5(c) until the threefold

coordinated sp^2 carbon atoms bind among themselves, so all the carbon bonds become sp^3 .

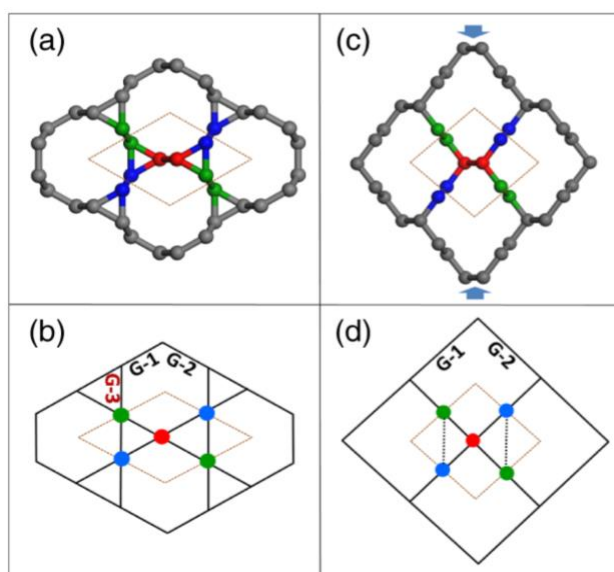


Figure 5. (a) CKL. The unit cell consists of six C atoms in the form of two linked triangles. Each pair of the (same color) atoms forms a zigzag chain in the vertical direction. (b) A schematic Kagome lattice for the CKL, where G-1, G-2, and G-3 denote three interlocked graphene sheets. Notice that each lattice point in the 2D structure here represents a zigzag chain in the perpendicular direction of the real structure. (c) and (d) Same plots for IGK. Notice the lack of G-3 in an IGK.

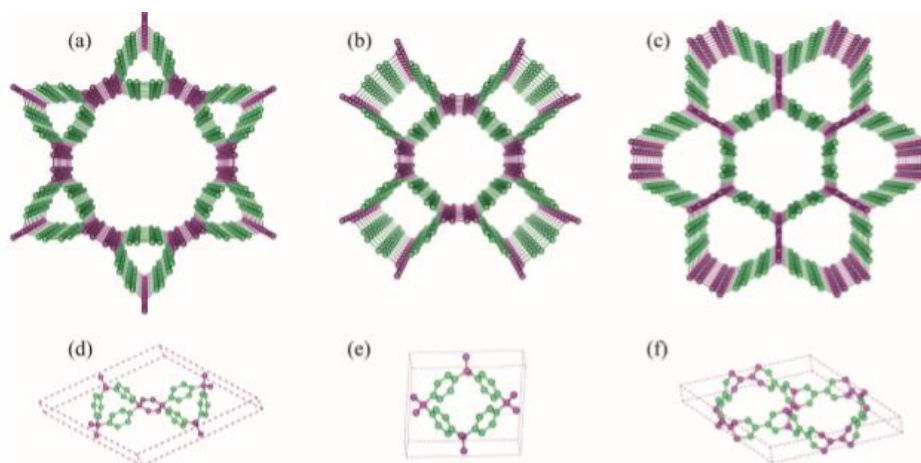


Figure 6. Graphene networks made of zigzag-edged GNRs: TGN(2,2), QGN(2,2), and HGN(2,2), by a direct link. (a-c) Top views of the networks and (d-f) tilted views of the corresponding unit cells.

The closely packed structures in Fig. 5 are in fact only the tip of the iceberg, as one can make a whole series of structures by replacing the colored dimers in the figure or a single row of zigzag carbon chains by GNRs of variable widths^{52,130}. Here, (zigzag-edged or armchair-edged) GNRs are linked to each other either directly as in Fig. 5 or via a row of carbon atoms (see below). Figure 6 shows three

carbon networks where two kinds of zigzag-edged GNRs of m rows (green) and n rows (purple) are linked together directly¹³⁰. They have been classified as a triangular graphene network (TGN) [Fig. 6(a)], a quadrilateral graphene network (QGN) [Fig. 6(b)], and a hexagonal graphene network (HGN) [Fig. 6(c)]. By changing the widths of green and purple nanoribbons, one arrives at three families of graphene networks, TGN(m,n), QGN(m,n), and HGN(m,n).

The family of carbon honeycomb (CHC) represents 3D networks where the zigzag-edged nanoribbons are connected by a row of joint carbon atoms or dimers. From the top view, these structures look like honeycombs, as can be seen in Fig. 7(a). Here, again we use different colors to denote different carbon atoms: e.g., green and blue denote C1 atoms with a sp^2 electronic configuration, while orange denotes the joint C2 atoms. The C1 atoms can be further divided into two subgroups, i.e., green and blue; together they form the zigzag chains along the c axis, while each subgroup resides on a different horizontal plane [see Figs. 7(b-c)]. The C2 atoms may form dimers to become sp^3 or remain un-dimerized and are hence sp^2 . The former is termed CHC- I with the primitive cell shown in Fig. 7(b), while the latter is termed CHC- I' with a $2x$ primitive cell shown in Fig. 7(c) for comparison. Similar to CKLs and IGNs, one can increase the width of the nanoribbons from $n = 1$ to CHC- n with $n > 1$.

Krainyukova and Zubarev obtained CHC in 2016 by a deposition of vacuum-sublimated graphite where carbon was evaporated in vacuum from thin carbon rods heated by an electric current¹³¹. The carbon films obtained have a thickness in the range of 80-100Å. They were analyzed by means of transmission electron microscopy (TEM) [see Fig. 7(d) (left)] and low temperature high energy electron diffraction. The authors claimed that a careful and thorough analysis excludes carbon nanotubes and other carbon forms, so the only possibility is the carbon honeycomb shown in Fig. 7(d) (right). To our knowledge, this is perhaps the first experimental highly-ordered 3D carbon network made of predominantly graphene nanoribbons. With future technological improvements, we believe the theoretically-predicted carbon structures such as those in Figs. 4 and 5 will also be realized in the future.

Besides the graphene networks or carbon foams^{52,132-143}, other 3D carbon allotropes that have been proposed previously include the Mackay crystals¹⁴⁴⁻¹⁶³.

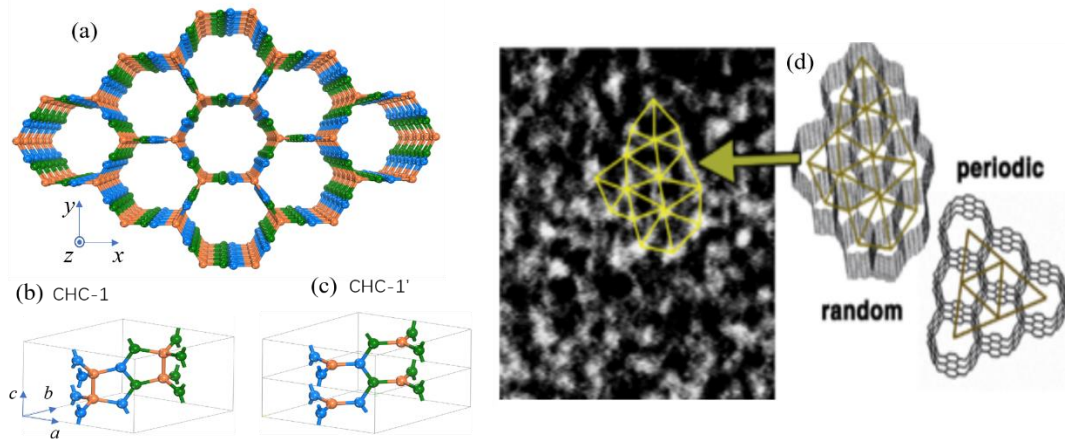


Figure 7. Carbon honeycombs. (a-c) Atomic structures: (a) CHC-1 in a top-view perspective, where the carbon atoms form a 3D honeycomb. (b) Primitive cell of CHC-1 in a side view perspective, where the green C1 and blue C1 atoms reside on different horizontal planes with respect to the c axis. Each kind of C1 atoms has a threefold rotational symmetry with respect to the axes passing through the orange connecting C2 dimers. In (a) and (b), t_0 to t_5 are the tight-binding hopping parameters. (c) An alternative to CHC-1, namely, CHC-1' in a $1 \times 1 \times 2$ supercell where the C2 dimerization has been lifted. (d) An experimentally synthesized CHC structure (left). Both random and ordered honeycomb structures (right) have been claimed.

III. Topological phases in general

The recent studies of topological properties of materials is one of the most active research areas currently in condensed matter physics^{164,165}. Beginning with topological insulators and especially the more recent studies of topological semimetals/metals (TMs) have been the subjects of a great deal of research. TMs are characterized by a topologically stable Fermi surface originating from a crossing of energy bands. Band crossings of this kind can be associated with a topological number¹⁶⁶⁻¹⁷⁰, which may depend on the symmetries responsible for enforcing or protecting the degeneracy at the band crossing. Based on the codimension of the band crossings, three types of topological phases have been proposed¹⁷¹⁻¹⁷³, i.e., nodal point, nodal line, and nodal surface. In the nodal-point semimetals, the conduction and valence bands cross each other at zero-dimensional (0D) discrete points¹⁷⁴⁻¹⁸³, which include the Weyl point¹⁷⁴, triple point¹⁷⁸⁻¹⁸⁰, Dirac point¹⁷⁵⁻¹⁷⁷, and multifold-degeneracy points¹⁸³ (see for example Fig. 7). In the nodal-line semimetals¹⁸⁴⁻²⁰¹, the band crossings form 1D lines in momentum space, instead of discrete points. Because lines can be deformed into many different shapes (e.g., a

ring or a knot), there exist diverse topological phases for the nodal lines²⁰²⁻²¹⁸, such as nodal chains, nodal links, and Hopf chains, etc. In the third type of TMs, the band crossings form a 2D surface^{51,219-222}, where each point is a crossing point whose dispersions are linear along the surface normal direction. The nodal surfaces can also have many variations such as being planner or spherical.

TMs can exhibit a variety of different low-energy excitations which offer a new platform for fundamental studies of novel quasiparticles which differ from the known particles in high-energy physics²²³⁻²²⁵. Due to the nontrivial topology of bulk and surface electronic states, TMs are expected to exhibit some novel properties²²⁶⁻²³¹, such as nearly flat drumhead-like surface states²²⁶, unusual magnetoresistance²³⁰, and a chiral anomaly²³¹, which have attracted attention from both theoretical and experimental perspectives. Moreover, TMs are of broad interests due to their potential applications in chemical catalysis^{232,233}, quantum computation^{234,235}, and spintronics²³⁶⁻²³⁸, to name a few. In the following, we will introduce some typical TMs.

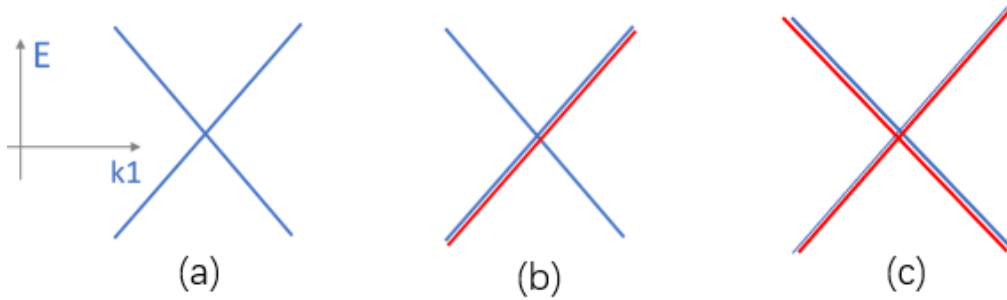


Figure 8. Three basic types of nodal points. (a) Weyl point, (b) triple point, and (c) Dirac point.

3.1 Nodal points

As mentioned above, there are three classes of degenerate points in nodal-point semimetals. According to the band dispersions, these points can be further classified into type I and II²³⁹⁻²⁴¹.

Dirac point:

The Dirac point is the first-proposed topological element in TMs²⁴¹⁻²⁴⁸. It is a critical phase between the normal and topological insulator phases²⁴⁹. The Dirac Hamiltonian can be expressed as a 4×4 matrix⁸⁹:

$$H(\mathbf{k}) = v\mathbf{k} \cdot \boldsymbol{\sigma}\tau_x + m\tau_z = \begin{pmatrix} m & v\mathbf{k} \cdot \boldsymbol{\sigma} \\ v\mathbf{k} \cdot \boldsymbol{\sigma} & -m \end{pmatrix}, \quad (1)$$

where $\mathbf{k} = (k_x, k_y, k_z)$ is the momentum, v is the velocity, and m is the mass; $\boldsymbol{\sigma} = (\sigma_x, \sigma_y, \sigma_z)$ and $\boldsymbol{\tau} = (\tau_x, \tau_y, \tau_z)$ are both Pauli matrices. When the sign of m is changed, the topology of the ground state transitions from a normal insulator to a topological insulator. At the critical point of the transition ($m = 0$), the Hamiltonian is gapless at $\mathbf{k} = 0$, corresponding to a point node with fourfold-degeneracy and linear dispersion. The Dirac point of the massless Dirac equation is shown in Fig. 8(c).

Weyl point:

In Eq. (1), when $m = 0$, the Dirac Hamiltonian decouples into two separated Weyl equations given by $\pm v\mathbf{k} \cdot \boldsymbol{\sigma}$. Each Weyl equation describes a two-component chiral Weyl fermion with chirality ± 1 ^{250,251}. In general, a two-component Weyl fermion described by the Weyl equation arises when two non-degenerate energy bands in a solid touch at a point k_0 in momentum space [see Fig. 8(a)]. Clearly, this cannot happen when Kramers degeneracy holds at every momentum \mathbf{k} . Therefore, time (T) and parity (P) symmetry cannot be simultaneously satisfied; at least one of these must be broken^{252,253}. The topology of Weyl fermions follows from the fact that Weyl points are monopoles of momentum-space Berry curvature²⁵⁴⁻²⁵⁶. Therefore, in a system with only chiral Weyl fermions, the Weyl points must come in pairs of opposite monopole charges^{257,258}. [This explains, for instance, why the massless Dirac equation of Eq. (1) decouples into two Weyl equations with opposite chirality.]

Triple point:

In solid state systems, three-, six-, and even eight-fold band crossings can be observed which yields low-energy fermionic excitations that cannot be described by a Dirac or Weyl equation^{183,259-261}. Instead, their dispersions have to be described by a more general Hamiltonian²⁶². The departure from the (low-energy) description of familiar relativistic free fermions (i.e., Dirac and Weyl fermions) is a consequence of the less-restrictive nature of crystal symmetry. On the other hand, it allows for the realization of more low-energy fermions (which otherwise do not exist). These TMs, characterized as “multifold” (i.e. three-, six-, and eight-fold) fermions are symmetry-enforced semimetals, as their very existence relies on the fundamental constraints originated from the space group symmetry²⁶³, possibly combined with T symmetry. For example, a crystal having a threefold rotational axes and point-group symmetry C_{3v} can be a “triple-point” semimetal²⁶⁴⁻²⁶⁹. The origin of the triple-point semimetals is

rooted in the band inversion between a single and doubly degenerate bands (see Fig. 8(b)).

3.2 Nodal lines

In 3D, two bands can cross each other along a closed curve or at a surface at discrete Dirac or Weyl points, as discussed above. When it is a curve, the curve is called a nodal line²⁷⁰⁻²⁷⁸, which may either take the form of an extended line running across the Brillouin zone (BZ), whose ends meet at the BZ boundary¹⁸⁴, or wind into a closed loop inside the first BZ²⁷⁶, or even form a chain consisting of several connected loops (nodal chains)²¹⁷. Topological semimetals with such line crossings are called topological nodal-line semimetal²⁷⁹⁻²⁸⁴. Nodal-line degeneracies can take place when energy bands of different crystal symmetries cross along a rotational axis, or on a mirror- or glide-invariant plane of the BZ^{213,285-288}. In addition, nodal lines can also occur as a result of band topology, in which the nodal lines are associated with a topological invariant²⁸⁹⁻²⁹¹. A variety of topological nodal-line semimetals have been identified with distinct characteristics (unique to each class) such as topological invariants, degeneracy at the band crossing, Fermi surface geometry, and the linking structure of the multiple nodal lines²⁹²⁻²⁹⁶.

Compared with nodal-point semimetals, nodal-line semimetals have more subtypes because a line can deform in many ways, such as forming a ring or a knot^{212,297-299}. If there are two or more lines/rings of different origins in momentum space, they can construct even more topological phases³⁰⁰⁻³⁰⁷. Figure 9 depicts several basic topological elements made of nodal rings. For example, Fig. 9(a) is an isolated nodal ring; Figs. 9(b-c) are intersecting nodal rings (INRs), in which all the rings share a common center; Fig. 9(d) is a nodal chain, where the nodal rings contact each other in a sequential manner and extend across the BZ to form a chain; Figs. 9(e-f) show nodal link and Hopf link, respectively, in which the nodal rings are topologically linked together. Note that one of the rings in the Hopf link crosses the boundaries of the BZ, making it distinct from the standard nodal link in Fig. 9(e).

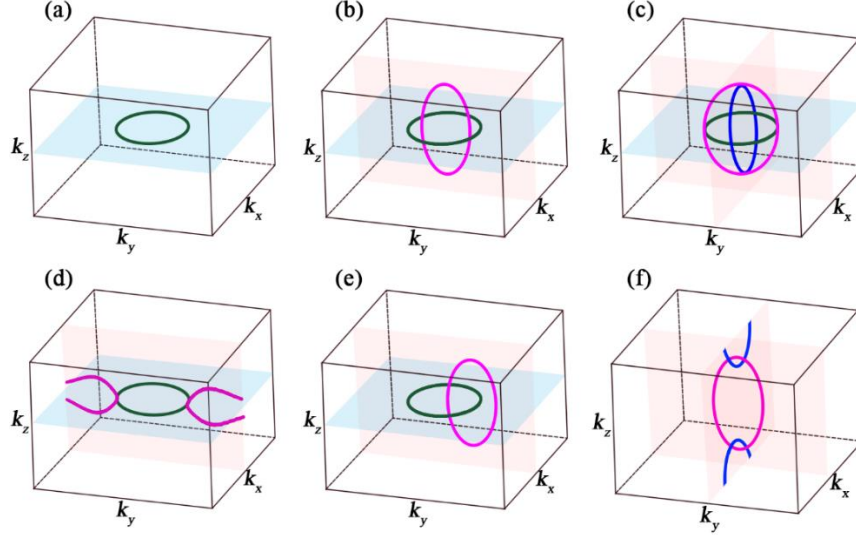


Figure 9. Topological elements consisting of nodal lines (or nodal rings). (a) An isolated nodal ring; (b-c) intersecting nodal rings (INRs) of two and three rings, respectively; (d) a nodal chain; (e) nodal link, and (f) Hopf link.

3.3 Nodal surfaces

Besides points and lines, band crossing in a 3D BZ can also take the form of a 2D nodal surface^{50,51,222,308,309}. On such a surface, each point is a crossing point of two linear bands in the direction normal to the surface. The nodal surface is distinct from the ordinary Fermi surface, because the coarse-grained quasiparticles excited from a nodal surface have an intrinsic pseudospin degree of freedom (representing the two crossing bands), behaving effectively like a 1D massless Dirac fermions along the direction normal to the surface, and may therefore have interesting physical properties.

The nodal surfaces can be planar surfaces or have a spatial shape such as forming a sphere³⁰⁸, as depicted in Fig. 10. Around the surfaces, low-energy quasiparticles can be described by an effective Hamiltonian⁵¹

$$H(k_z) = \tau_z v k' \sigma_z, \quad (2)$$

where $k' = k - k_0$ is the wave vector component normal to the nodal surface with k_0 the vertical distance from the surface to the center of the BZ, v is the Fermi velocity, and σ_z (the Pauli matrix) denotes the two bands crossing at the surface.

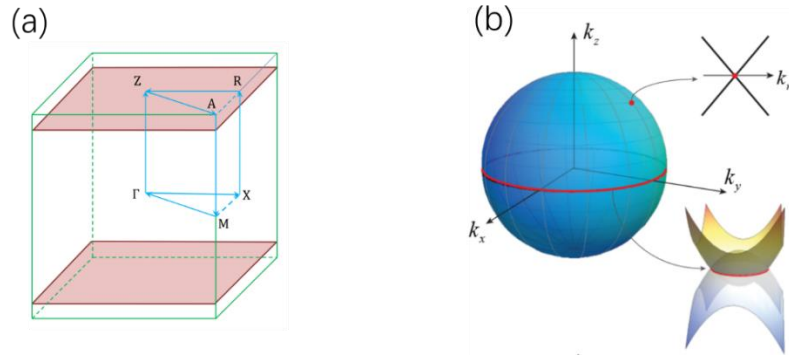


Figure 10. (a) A planner and (b) a spherical nodal surfaces.

IV Topological properties of carbon

4.1 Orbital physics in the graphene-based structures

Electrons in an isolated atom are characterized by their charge, spin, and orbital character³¹⁰. When these atoms form a solid, mutual interactions and entanglements of these can lead to the determination of material properties. One can manipulate one or more of the above to achieve desired goals. For example, charge is associated with electrical conductivity and spin with magnetism³¹¹. Usually, electrons in the outer-shell orbitals are most important to most of the physical and chemical properties of a solid. Due to the orthogonality requirement in quantum mechanics, different atomic orbitals must have different wave function shapes³¹². For instance, while an s orbital is spherical and an even function with respect to the origin, the next higher-energy p orbitals are non-spherical and odd functions with respect to the origin. The spherical symmetry of an atom determines that there are only three such p orbitals degenerate in energy, which form the basis for the topological properties of carbon. From an electronic structure point of view, within the tight-binding model^{313,314}, all the band structures are determined by the interplay between the s and p orbitals of the valence electrons inside the crystal and the spatial symmetry of the crystal.

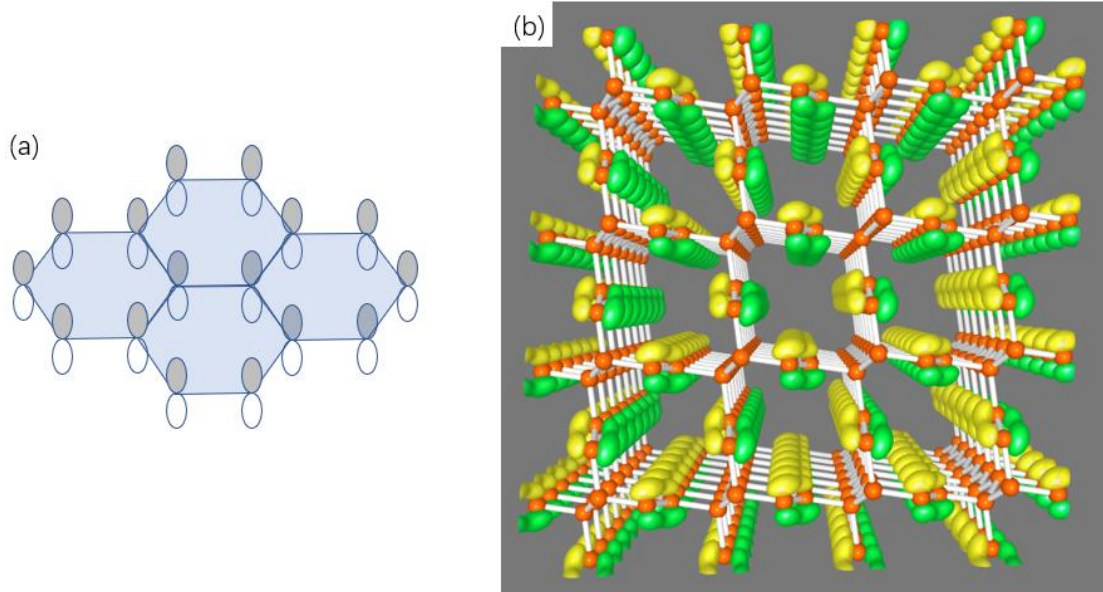


Figure 11. (a) An in-phase p_z orbital configuration in graphene. (b) The distribution of p orbitals in an IGN.

Carbon has six electrons, of which the four outer-shell electrons $2s^2 2p^2$ are the valence electrons. A carbon atom can thus have sp , sp^2 , or sp^3 hybridization to form a variety of allotropes of different bonding configurations³¹⁵. Graphene may be viewed as a 2D π -conjugated material, in which the sp^2 -hybridized carbon atoms are arranged such that they form a 2D hexagonal lattice composed of benzenoid rings³¹⁶ [see Fig. 11(a)]. On the other hand, its delocalized π -conjugated electrons in the hexagonal lattice yield a unique band dispersion, i.e., a Dirac dispersion near the Fermi level (E_F)^{317,318}. This is important for our discussion, because in most graphene-based 3D structures, the electronic properties are dominated by atomic p orbitals similar to the p_z orbital in graphene^{43,51,52,319,320}. For example, Fig. 11(b) shows the wavefunctions of electrons near the E_F in a 3D IGN³⁶, where the p_z orbitals of graphene become p_x and p_y orbitals if we take the perpendicular direction out of page as the z axis. Other lattices can also accommodate the p_z orbitals of graphene in a similar manner to produce rich physical properties as the interactions among these orbitals will be lattice- and atomic structure-dependent^{51,321}. To envision such situations, especially when the relative phases between neighboring orbitals matter, it makes sense to treat these p orbitals as a rank-1 tensor (or vector) with a clearly-defined polarity (e.g., pointing from its negative lobe to positive lobe), in analogy to a spin vector^{322,323}. If these vectors are placed in a Kagome lattice (such as in the CKL discussed earlier), the so-called “spin frustration” will occur¹²⁹. In other words, these p orbitals will not be able to arrange themselves

to yield a long-range “antiferromagnetic” ordering in their respective phases¹¹⁵.

4.2 Topological properties of graphene nanoribbon junctions

Like graphene, the electronic structure of 1D GNR has interesting topological properties³²⁴⁻³²⁹. The exact electronic topology is, however, determined by the spatial symmetry and termination at the edges. Hence, GNRs of different widths, edge shapes, and end termination geometries belong to different topological classes³²⁴.

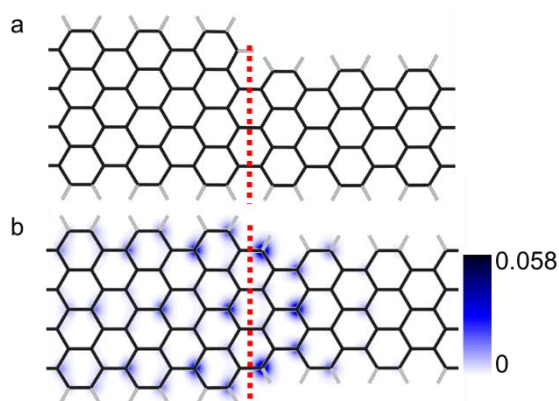


Figure 12. Heterojunctions formed between two topologically (a) equivalent and (b) inequivalent $N=9$ and $N=7$ armchair GNRs (9AGNR/7AGNR). Red dashed lines denote the interfaces. The carbon-carbon and carbon-hydrogen bonds are colored black and gray, respectively. The color scale shows the charge density of the localized midgap junction state. The charge density is integrated along the out-of-plane direction [in units of $1/(\text{a.u.})^2$].

Joining two GNRs of different topological classes leads to localized junction states at their interfaces³²⁹. Here, the bulk-boundary correspondence in armchair GNR heterojunctions is shown, which are experimentally accessible by bottom-up synthesis with precursor molecules. Figure 12(a) show two possible types of junctions formed by an $N=7$ armchair GNR and an $N=9$ armchair GNR. For the nonsymmetric junction, both $N=7$ and $N=9$ armchair GNR segments have a zigzag termination, and they are topologically equivalent. As a result, no localized junction states can be found at the interface. For the symmetric junction [Fig. 12(b)], however, the termination of the $N=7$ armchair GNR changes, so the two GNRs become topologically inequivalent. As a result, one localized junction state emerges in the band gap³²⁹.

4.3 Dirac points in 2D carbon sheets

Graphene is perhaps the most well-known 2D Dirac material with two Dirac points located at K and K' points of the BZ, energy E_F , as shown in Fig. 13(a) for K^{97,330,331}. Near the E_F , electrons behave as if they have no mass, resulting in energies that are proportional to the momentum of the electrons. There have been different classes of materials possessing such distinctive electronic properties: besides graphene, noticeably the high-temperature *d*-wave superconductors^{332,333} and topological insulators^{164,334}.

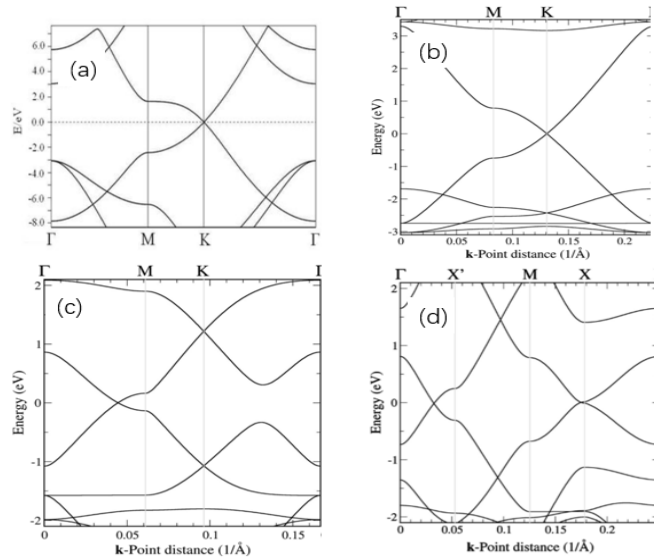


Figure 13. Band structures of graphene and graphynes: (a) graphene, (b) α -graphyne, (c) β -graphyne, and (d) 6,6,12-graphyne. All exhibit characteristic Dirac points at E_F .

In this regard, it is worth noting that the three graphynes in Fig. 3 are also Dirac materials³³⁵⁻³³⁸, as can be seen in Figs. 13(b-d). By examining Fig. 3, we conclude that the introduction of the triply-bonded *sp* carbon atoms do not affect the Dirac cones, which originate from the *sp*² carbon networks. Thus, similar to graphene, Fig. 13(b) shows that hexagonal α -graphyne has a nearly isotropic electric property near the E_F at K point⁹⁷. However, such an isotropy is lost when the symmetry of the crystal is altered as in the case of β - and 6,6,12-graphynes where the Dirac points do not reside at any high symmetry points of the BZ⁹⁷. In the case of rectangular 6,6,12-graphyne, the symmetry change even alters the relative energy positions between the Dirac point along X'- Γ and that along X-M⁹⁷. This energy shifts make one Dirac cone slightly above the E_F , while the other slightly below the E_F , which enables a self-doping of the graphyne to result in spontaneous electron and hole pockets. This self-

doping effect can be further tuned by applying an in-plane strain.

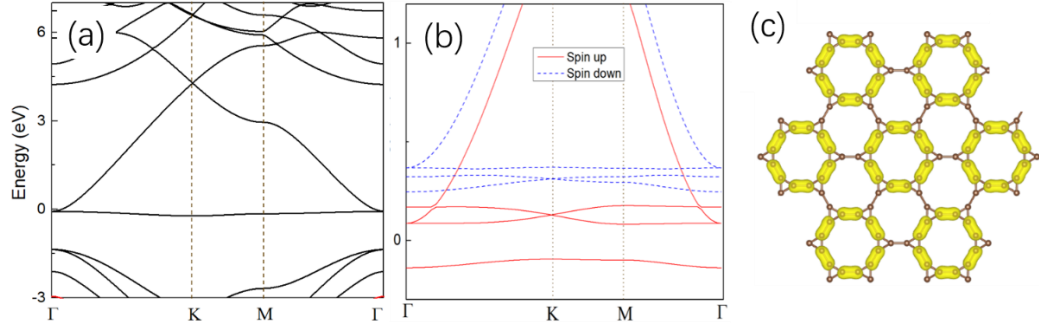


Figure 14. (a) Band structure of the Kagome graphene in Fig. 4(a). (b) Band structure of the Kagome graphene in the $\sqrt{3} \times \sqrt{3}$ supercell as a result of hole doping with a filling factor for the flat band of $1/6$. (c) Charge density contour for states in the occupied flat band in panel (b), showing a Wigner crystallization.

In a Kagome lattice in Fig. 4(a), there exist the so-called Kagome bands, each of which consists of two Dirac bands plus a flat band as can be seen in Fig. 14(a)¹¹¹. Here, the flat band appears right below the E_F . The two Dirac bands, which connect the flat band at the Γ point, cross each other at the K point, forming a Dirac point but at a considerably higher energy. The flat band is fully occupied while the two Dirac bands are empty. Interaction in a flat band is magnified due to the divergence in the density of states, which gives rise to a variety of many-body phenomena such as ferromagnetism, Wigner crystallization, and anomalous quantum Hall effect¹¹¹. Upon hole doping, the flat bands will split into spin-polarized bands of different energies to result in a flat-band ferromagnetism [see Fig. 14(b)]. In particular, at a half filling $\nu = \frac{1}{2}$, the splitting reaches the maximum value of 768 meV. At smaller fillings, e.g., when $\nu = \frac{1}{6}$, on the other hand, a Wigner crystal spontaneously forms, as shown in Fig. 14(c), where the electrons form closed loops localized on the grid points of a regular triangular lattice¹¹¹. As expected, it breaks the translational symmetry of the original Kagome lattice.

4.4 Topological properties of 3D carbon allotropes

Dirac/Weyl loops and points in IGN

Figure 15(a) shows that each primitive cell of an IGN contains six C atoms, which form two separate obtuse triangles symmetrically placed with respect to the inversion center of the cell³⁶.

Chemically, the six atoms also belong to two different groups: the two near the inversion center (marked grey) are fourfold coordinated; and the other four (marked red) are threefold coordinated.

In the band structure in Fig. 15(b), linear dispersions near the E_F along the Γ -Z, Y-T, and Y'-T' symmetry lines are observed. A closer examination of the BZ in Fig. 15(c) reveals that the linear band crossings take place along two closed loops traversing the BZ in the (110) mirror invariant plane around $k_c = \pm 0.45\pi/c$, as shown in Fig. 15(d). The two loops are in fact time-reversal and inversion images of each other.

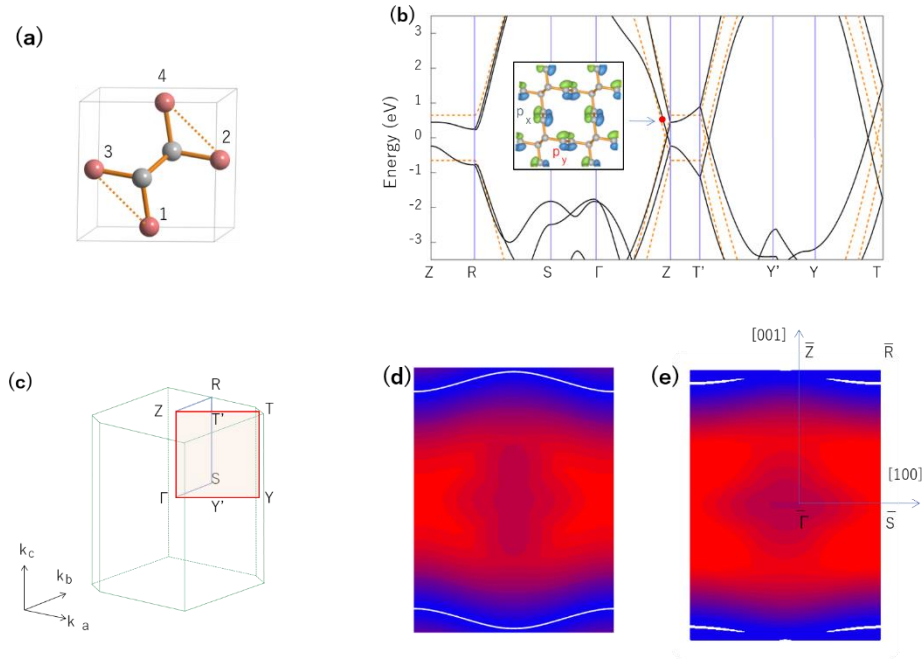


Figure 15. Electronic structure of IGN. (a) Primitive cell, (b) energy dispersion, (c) BZ, (d) Dirac/Weyl loops on the $k = k_a = k_b$ surface, and (e) Fermi arcs between Weyl points.

A charge analysis [see inset of Fig. 15(b)] reveals that the bands near E_F are mainly made of the p_x and p_y orbitals of the π -bonds, spatially located on only one type of the atoms, i.e., the four (orange) peripheral carbon atoms in Fig. 15(a)³⁶. Thus, the local atomic structure, the linear dispersion, and the π -bond character of the states are all reminiscent of the 2D graphene. If we ignore the small dispersion along $k = k_a = k_b$ in Fig. 15(d), the energy spectrum near E_F may be viewed as derived from a superposition of non-interacting 2D graphene sheets stacked in the [110] direction.

To capture energy dispersions near the E_F , one may construct a minimal tight-binding model that includes the four peripheral carbon atoms with one p orbital each (either p_x or p_y depending on the

locations)³⁶,

$$\mathcal{H}(\mathbf{k}) = \begin{bmatrix} 0 & Q(\mathbf{k}) \\ Q^\dagger(\mathbf{k}) & 0 \end{bmatrix}, \quad \text{with } Q(\mathbf{k}) = \begin{bmatrix} f_{14} & f_{13} \\ f_{24} & f_{23} \end{bmatrix}, \quad (3)$$

where $f_{ij}(\mathbf{k}) = \sum_\mu t_{ij} e^{-ik \cdot \mathbf{d}_{ij}^\mu}$, $i, j \in \{1, 2, 3, 4\}$ are the site labels in Fig. 15(a), t_{ij} is the hopping strength between sites i and j , \mathbf{d}_{ij}^μ is the vector directed from j to i , and μ runs over all equivalent lattice sites under translation. The spectrum of the energy band is symmetric about zero energy because of the presence of a chiral (sublattice) symmetry $\mathcal{C} = \sigma_z \otimes \sigma_0$ in Eq. (3), such that $\mathcal{C}H\mathcal{C}^{-1} = -H$ is independent of \mathbf{k} , where σ_α are the Pauli matrices. It is easy to show that zero-energy states would appear if the following two conditions are met: (1) $k_a = k_b$ and (2) $\cos(k_c c/2) = \sqrt{t_{13}t_{24}/(4t_{14}t_{23})}$. The first condition restricts the zero-energy states to the mirror invariant plane, whereas the second one further restricts them onto two separate loops at $\pm K_c = (2/c)\text{arc cos}[\sqrt{t_{13}t_{24}/(4t_{14}t_{23})}]$.

The inversion symmetry of the IGN may be destroyed by inserting (chemically inert) helium atoms into the interstitial sites or holes in Fig. 5(c), with a filling of one He per primitive cell³⁶. This will result in four Weyl-like points. We use the phrase Weyl-like here, because in our discussions the spin degree of freedom never enters due to the exceedingly small spin-orbit coupling of carbon. Once the Weyl-like points are created, they are topologically protected by the Chern number of any constant-energy surface enclosing these points. If we have an open system with surfaces, surface Fermi arcs must emerge, connecting the surface-projected Weyl-like points of opposite chirality. This is indeed the case as can be seen in Fig. 15(e) where the Fermi arcs on the (100) surface are shown³⁶.

Classification of nodal rings: the case for armchair graphene networks

Figure 16(a) shows an atomic structure of the carbon networks formed by connecting armchair GNRs, named AGNW- (m, n) ³³⁵. Variations in m and n produce a series of networks. At the shared atomic lines are the gray atoms, which are all sp^3 hybridized, while inside the nanoribbons are the

unshared blue C_1 and pink C_2 atoms, which are all sp^2 hybridized. The space groups of AGNW-(3,2) and (1,2) are both IMMA with a mirror plane M_z normal to the z axis.

First-principles calculations of AGNW-(3,2) and (1,2) reveal three different types of nodal rings, whose characteristic energy dispersions are schematically shown in Figs. 16(b-d)³³⁵. Both type-I and II rings may be viewed as a crossing line between two paraboloids as indicated by the green lines in Figs. 16(b-c). The opening of the paraboloids is always along the energy axis, either positive or negative: if they are in the opposite directions, one gets a type-I ring, if they are in the same direction, however, one gets a type-II ring, in accordance with the definitions of type-I and II Dirac points. On the other hand, a type-III ring emerges when a crossing between a paraboloid and a saddle surface takes place, as shown in Fig. 16(d), in which along k_y the Dirac point is type-I but along k_x the Dirac point is type-II.

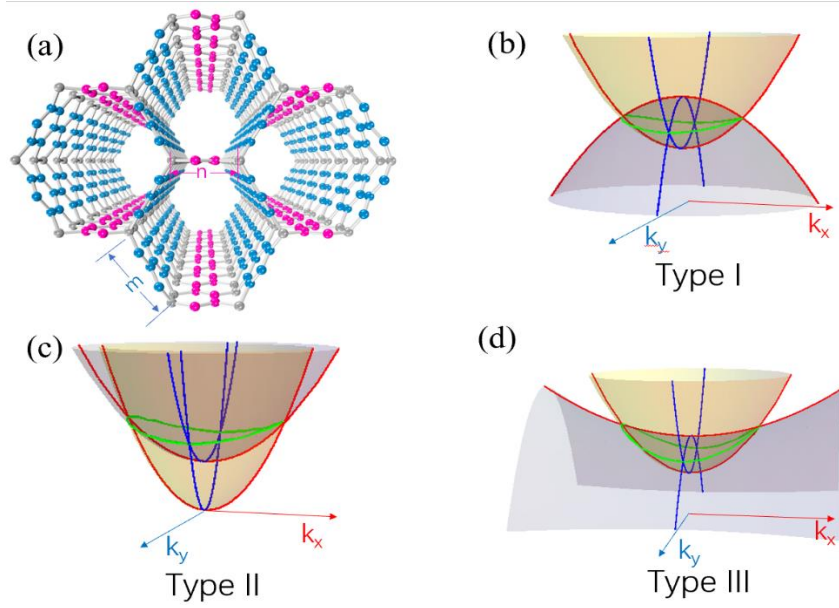


Figure 16. (a) Atomic structure of AGNW-(m,n), (b) type-I, (c) type-II, and (d) type-III nodal rings. All three types can be found in AGNW-(3,2) and (1,2) under a strain.

Since the classification only requires knowledge on the curvature of the energy bands, it can be straightforwardly obtained by a $k \cdot p$ model up to quadratic terms in k , in this case at the Γ point³³⁵:

$$H(\mathbf{k}) = \begin{bmatrix} A_1 k_x^2 + B_1 k_y^2 & iCk_z \\ -iCk_z & \Delta + A_2 k_x^2 + B_2 k_y^2 \end{bmatrix}, \quad (4)$$

where Δ is the band gap, and A_1 , B_1 , A_2 , B_2 , and C are band parameters obtained by fitting to the DFT

results. By a change in the signs of these parameters, all three types of nodal rings (discussed above) are obtained.

Note that the electron hole pockets arising from the Hamiltonian in Eq. (4) exhibit a rich variety of patterns, which can serve as a platform to study fundamental electronic and magnetic properties of the rings such as anisotropy in electron/hole transport and collapse of Landau levels³³⁵. It is known that the nodal rings are subject to a (Lifshitz) phase transition, through which the electron hole pockets gradually evolve from one to the other – a phenomenon that may be used to study electron-hole friction and strongly-correlated Coulomb interactions in the flat-band region as a result of the transition³³⁶.

Dirac/Weyl surfaces

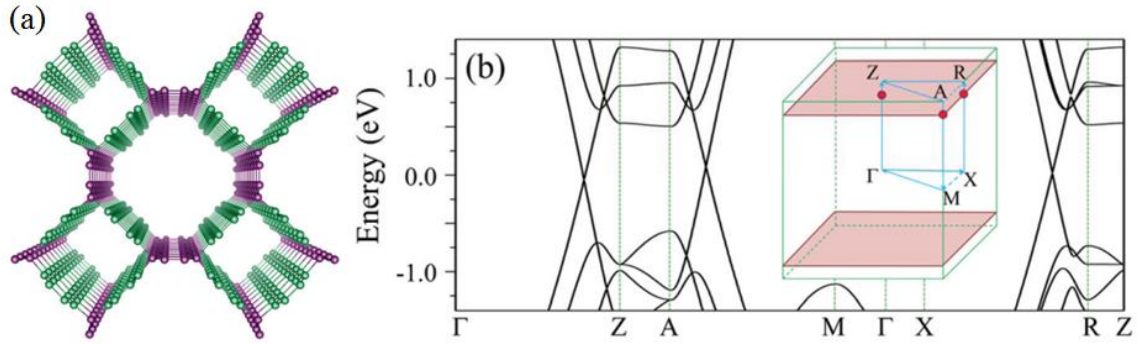


Figure 17. QGN(2,2). (a) Atomic structure and (b) energy dispersion near the Fermi level, where the pink-red-color-shaded planes are Weyl surfaces in the BZ.

Three types of graphene networks, TGN(2,2), QGN(2,2), and HGN(2,2), have been discussed in Fig. 6⁵¹. All of them are TMs with nodal-surfaces. Here, we will take the simplest case, QGN(2,2) in Fig. 17(a), to explain the electronic properties for all of them. One observes from the band structure in Fig. 17(b) that linear crossings at the Weyl-like points appear along each of the symmetry lines, Γ -Z, A-M, and X-R in the BZ, which are in fact the E_F . There are three of them, all marked on in the inset of Fig. 17(b) as red dots. Interestingly, all three points have a common $k_z = 0.39\pi/c$. In other words, they all lie on a flat Weyl surface, denoted in the inset by the pink-red plane. Because of time reversal symmetry, there should be another Weyl surface at $k_z = -0.39\pi/c$. It should be noted that here the Fermi surface passing the Weyl points is different from that of an ordinary metal in the sense that the low-energy quasiparticles here must be described by a two-component Weyl spinors⁵¹.

The existence of Weyl surfaces in graphene networks can be explained by orbital-orbital interactions⁵¹. In particular, the electronic states near the E_F originate from green-color nanoribbons in Fig. 17(a), which, together with the purple-color corner carbon atoms, may be viewed as deformed nanotubes with a square cross section, separated by the purple-color nanoribbons which have no contribution to the electronic states near the E_F . As such, the network can be viewed as a 3D bundle of carbon nanotubes. It is known that the nanotubes are 1D Weyl semimetals with a linearly crossing at E_F in their respective band structures³³⁹. It turns out that, when forming the carbon networks, the inter-tube coupling between the σ electrons in the x - y plane is rather strong, leading to significant dispersions, but that between the π electrons in the same x - y plane is negligible. The latter leads to the Weyl surfaces in the x - y plane, which are almost dispersionless, as can be seen in the inset in Fig. 17(b).

The Weyl surface is usually unstable unless it is protected by symmetry and/or topology. In the current case, the stability of the Weyl surface is guaranteed by sublattice symmetries originated from crystalline mirror symmetries along the x and y axes, inherent to the structure, or a combination of the two. Such carbon systems, due to a negligible spin-orbit coupling, fall within the BDI topological class with a 0D \mathbb{Z}_2 topological invariant defined at any point in the BZ with a local gap³⁴⁰⁻³⁴². The \mathbb{Z}_2 invariant just indicates whether the gap is inverted or not, when referenced to the normal band ordering in the atomic limit. In the graphene networks, the band gap is inverted ($\mathbb{Z}_2 = 1$) near the central region of the BZ, while un-inverted ($\mathbb{Z}_2 = 0$) near the Z-point at the boundary of the BZ. The Weyl surfaces, which separates these two regions of different band topologies, cannot be gapped, as long as the sublattice symmetry is maintained⁵¹.

Triple points and linked nodal rings in 3D pentagon carbon networks

Another class of carbon allotropes are the 3D pentagon carbon networks, one of which is shown in Fig. 18(a)³⁴³. It can be viewed as being formed by interlinking two orthogonal arrays of pentagonal-ring nanoribbons (red and blue, respectively), which are then stacked along the z direction. Upon linking, the two nanoribbons share one atom marked by green in Fig. 18(a). Similar to most of the 3D carbon networks, in the pentagon lattice, there are two kinds of carbon atoms, i.e. the sp^2 -hybridized red and blue atoms and the sp^3 -hybridized green atoms. The structure has the nonsymmorphic D_{4h}^{19}

space group (No. 141, $I4_1/AMD$), of which an important symmetry element is the screw \bar{C}_{4z} , which is a four-fold rotation along z , followed by a fractional translation of $c\hat{z}/4$, where c is the lattice parameter in the z direction³⁴³.

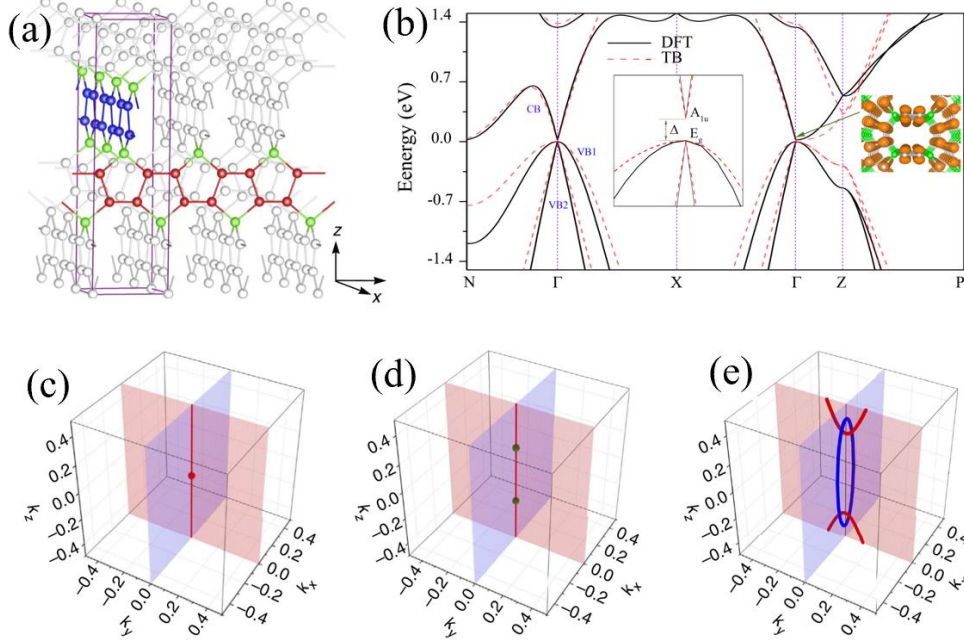


Figure 18. (a) Atomic structure of a 3D pentagon carbon, (b) the corresponding band structure by DFT (black lines) and TB (red dashed lines), and (c-e) topological phase transitions under strain from having only a single triplet point to having double triplet points to finally having a Hopf link.

The pentagon carbon networks are unique in topological physics because they produce a series of topological fermions beyond the usual Dirac and Weyl fermions^{176,252}. For example, the band structure in Fig. 18(b) shows that, under equilibrium, the network is a narrow-gap semiconductor. At Γ point and near E_F , there are two degenerate valence band states (heavy-hole and light-hole) and a single conduction band state only 21.4-meV higher in energy. In the vicinity of Γ , the light-hole valence band and the conduction band nearly cross linearly. The degeneracy of the two valence band states is a result of symmetry as they both belong to the 2D irreducible representation E_g of the D_{4h} group. In contrast, the conduction band state belongs to the 1D A_{1u} representation of the D_{4h} group. The two valence bands remain degenerate along Γ -Z (i.e., along the k_z -axis). This is because there is a smaller group C_{4v} along the screw axis, such that the 2D representation does not split. From an analysis of the wavefunctions and projected density of states (PDOS), one see that the band-edge states are mainly derived from the π orbitals of sp^2 carbon atoms.

Since the band gap is small, applying a tensile strain can increase the gap to produce a semiconductor, while a compressive strain can close the gap towards a semimetal. Of particular interest is the latter case when the band gap between the A_{1u} singlet and E_g doublet at Γ is closed, i.e., at the transition point. Due to the different symmetry characters, however, A_{1u} and E_g cannot hybridize with each other, which leads to the formation of the triplet point at Γ , as shown in Fig. 18(c)³⁴³.

After the transition point, if one applies strain further, the band order at Γ becomes inverted, while the order at Z remains the same. Such a band topology implies that the two bands must now cross each other between Γ and $\pm Z$. Furthermore, because the two bands belong to different representations along the screw-axis, they must cross in a linear manner, with two triply-degenerate points: one on each side of Γ as shown in Fig. 18(d). Therefore, the metallic phase of the pentagon carbon networks represents a novel TM phase with a pair of triply-degenerate band-crossing points near E_F .

To describe the above topological quantum phase transition near the band edges, a $\mathbf{k}\cdot\mathbf{p}$ model at Γ up to quadratic order is sufficient³⁴³:

$$H(\mathbf{k}) = (C + D_1 k_z^2 + D_2 k_\perp^2) + \begin{bmatrix} \Delta + B_1 k_z^2 + B_2 k_\perp^2 & -iAk_x & -iAk_y \\ iAk_x & 0 & B_3 k_x k_y \\ iAk_y & B_3 k_x k_y & 0 \end{bmatrix}, \quad (5)$$

where the coefficients A , B_1 , B_2 , C , D_1 , D_2 , and Δ are determined by fitting the DFT results. At the transition point, $\Delta = 0$, the three bands cross at a single point. To see what happens qualitatively, we may keep only the k -linear terms in Eq. (5). The following equation will result:

$$\mathcal{H}(\mathbf{k}) = A\mathbf{k} \cdot \boldsymbol{\lambda}, \quad (6)$$

where $\mathbf{k} = (k_x, k_y, 0)$, and

$$\lambda_x = \begin{bmatrix} 0 & -i & 0 \\ i & 0 & 0 \\ 0 & 0 & 0 \end{bmatrix}, \quad \lambda_y = \begin{bmatrix} 0 & 0 & -i \\ 0 & 0 & 0 \\ i & 0 & 0 \end{bmatrix}, \quad \lambda_z = \begin{bmatrix} 0 & 0 & 0 \\ 0 & 0 & -i \\ 0 & i & 0 \end{bmatrix}$$

are three of the eight Gell-Mann spin-1 matrices³⁴⁴, describing isospin-1 triplet fermions moving in the xy -plane^{259,343}. The fermions are helical with a well-defined helicity of ± 1 or 0, corresponding to the eigenvalues of a helicity operator $\mathbf{k} \cdot \boldsymbol{\lambda}/k$. The two branches with a helicity of ± 1 are massless, while the one with a helicity of 0 has a flat dispersion (= infinite mass).

Passing the critical point, the isospin-1 triplet splits into two triply-degenerate points at $k_z = \tau K_c$,

respectively, where $\tau = \pm$ and $K_c = \sqrt{-\Delta/B_1}$ according to Eq. (5). Note that to reproduce the DFT band structure in Fig. 18(b), one must have $\Delta < 0$ and $B_1 > 0$. The linearized model of Eq. (5) in this case becomes³⁴³:

$$H_\tau(\mathbf{q}) = \begin{bmatrix} 2\tau(B_1 + D_1)K_c q_z & -iAq_x & -iAq_y \\ iAq_x & 2\tau D_1 K_c q_z & 0 \\ iAq_y & 0 & 2\tau D_1 K_c q_z \end{bmatrix}, \quad (7)$$

where the wave vector \mathbf{q} is measured from the crossing point. One notes that in the direction perpendicular to the screw axis, i.e. in the q_x - q_y plane, the dispersion is the same as that for the isospin-1 triplet fermion in Eq. (6). In other words, the triply-degenerate fermions basically inherit the structure of the triplet fermion but acquire one more degree of freedom, i.e., motion along the z -direction. Meanwhile, their helicities are no longer strictly defined.

We stress that the two fermions discussed here, i.e., the isospin-1 triplet fermion and triply-degenerate fermion, are new quasiparticles. Unlike the Dirac and Weyl fermions, these fermions do not have a direct analogue in relativistic quantum field theory. Also, the isospin-1 triplet fermion point is not topologically protected, except that it marks the onset of a quantum phase transition. In contrast, the two triply-degenerate fermion points are protected by the nontrivial band topology as a result of the fourfold screw axis.

If one breaks the screw-rotational symmetry, the double-degeneracy of the E band will be lifted and the triply-degenerate fermions will disappear. However, the original A and E bands still have different characters under the mirror operations, M_{xz} and M_{yz} . As such, crossings between each of the split E band and the A band in the mirror-invariant k_x - k_z and k_y - k_z planes will still be protected, as long as the respective mirror symmetry is intact. For instance, by an additional uniaxial strain along x or along diagonal in the x - y plane, the resulting band crossings form two orthogonal concatenated Weyl loops with the topology of a Hopf-link. As an example, consider a tensile strain along x . Figure 18(e) shows that one Weyl loop is centered at Γ point lying in the k_x - k_z plane, while the other is centered at Z point lying in the k_y - k_z plane. It needs to be emphasized that a band crossing here only results in Weyl loop fermions, but not Weyl fermions, because the inversion symmetry is still intact. It should also be noted that there is no symmetry to pin these Weyl loops at a fixed energy, and indeed, along a loop the energy varies³⁴³.

Nexus network in carbon honeycomb structures

The CHC structures mentioned earlier also exhibit exotic fermions, as can be seen in Fig. 19, where Fig. 19(a) shows the band structure of CHC-1 along $\Gamma - A$ (in the k_z -direction)³²¹. At position α ($k_z = 0.07 \pi/c$ and $E = 0.50$ eV), the green and black bands cross. Again, here we will treat the real spin as a dummy variable because of its negligibly-small spin-orbit coupling. As such, the green band is a doublet, while the black band is singlet. Therefore, α is a triply degenerate point (TP).

There is another TP at $k_z = -0.07 \pi/c$, due to the inversion symmetry¹⁶⁴. The (green) doublet is a topological nodal line, which connect the two TPs. Due to the crossing at the TPs, however, the solid and dotted (green) doublets belong to different band index: solid = (-1, 0) and dotted = (0, +1), respectively. As can be seen in the schematic plot in Fig. 19(b), the solid nodal lines connect the TPs from the interior of k_z , while the dotted nodal lines connect the TPs from the exterior, namely, passing BZ boundaries in the k_z direction. Moreover, Fig. 19(b) shows that there are three mirror planes $k_y = 0, \pm\sqrt{3}k_x$ and hence there are three sets (denoted by different colors) of equivalent nodal lines 120° apart from each other. To zoom in, Fig. 19(d) shows the (0, +1) nodal lines in one mirror plane ($k_y = 0$), which form a nexus network. This is a standard connectivity for a nexus phase where the two TPs [to be denoted as nexus points (NPs)] are connected by four solid nodal lines, as well as by four dotted nodal lines.

Seen from Fig. 19(e), there are four (0, +1) nodal lines between the two NPs³²¹. Considering periodicity of the BZ, all the lines are actually linked each other and form a closed path. Therefore, the two NPs are not only connected by a straight line through Γ (corresponding to the solid green line in Fig. 19(a)), but also by a curved line. The curved line, which goes from one TP through β, Γ, β' and to the other TP, winds along the entire Brillouin torus as shown in Fig. 19(e). This kind of connectivity between the two NPs is called winding connectivity. The solid lines in Fig. 19(b) show schematically the NPs and the connecting (0, +1) nodal lines in the first BZ, which form a novel 3D nexus network.

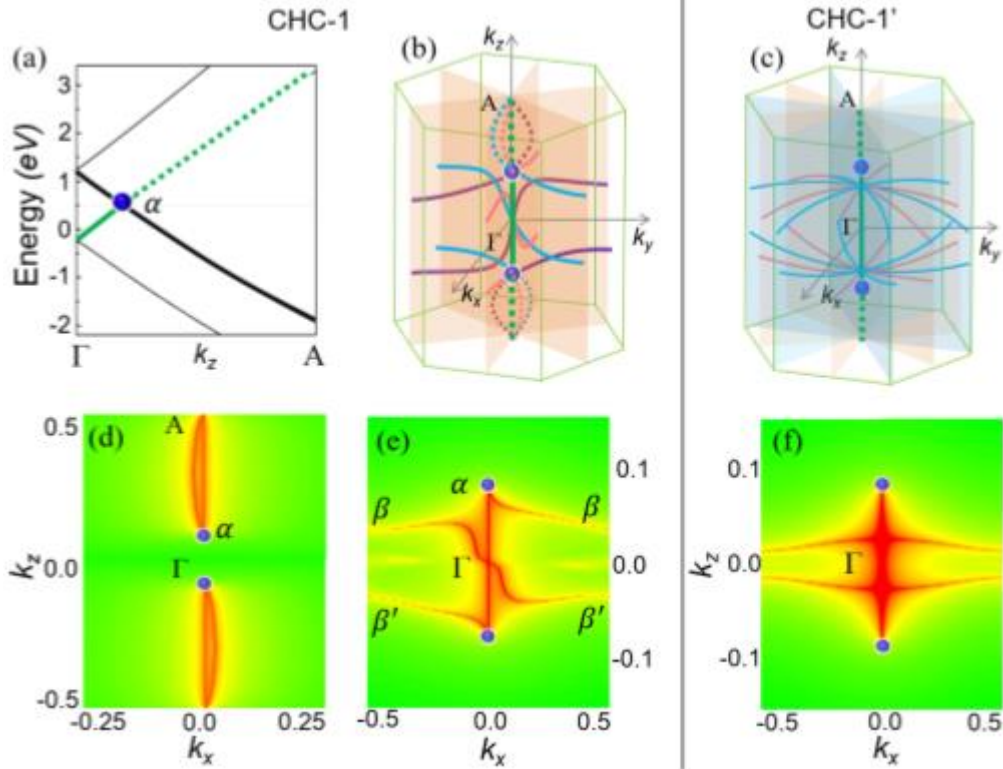


Figure 19. Topological properties of CHC-1 (a, b, d, e) and CHC-1' (c, d). (a) Band structure of CHC-1 along $\Gamma - A$ consisting of a green doublet and a black singlet band near the E_F . The blue point α is a TP at which the doublet and singlet cross each other. The doublet is the nodal line. Going from Γ to A and before the TP, the nodal line (green solid line) is made of two lower bands, denoted as $(-1, 0)$. After the TP, however, the nodal line (green dotted line) is made of two higher bands, denoted as $(0, +1)$. From the point of view of topology, however, they are two different classes of nodal lines. (b) Schematic illustration of the nexus network of CHC-1 in the first BZ. Solid lines correspond to the $(-1, 0)$ nodal lines, while dotted lines correspond to the $(0, +1)$ nodal lines. Orange planes are three mirror planes. (c) Schematic illustration of nodal lines of CHC-1' in the first BZ. Here due to the structural change, the nexus network in (b) is replaced by two simple sets of nodal lines along $\Gamma - A$. However, additional nodal lines (ANLs) emerge primarily in the k_x - k_y plane (i.e., being “planar”): besides the planar nodal lines associated with three (orange) mirror planes, there is equal number of planar nodal lines associated with three (light-blue) glide planes. They intersect with the nodal lines along $\Gamma - A$ at k_x - k_y plane. Due to crystal symmetry, these planar nodal lines are also symmetric with respect to k_z axis. (d) Contour map of the energy difference on the $k_y = 0$ mirror plane of the $(0, +1)$ bands for CHC-1. Red lines are where the energy difference is zero, i.e., on the nodal lines. The map shows a standard connectivity between the two TPs (also known as NPs). (e) Same as in (d) of the $(-1, 0)$ bands. The zoomed-in view for $k_z = (-0.2, 0.2)$ shows a winding connectivity between the two NPs. (f) Same as in (e) of the $(-1, 0)$ bands for CHC-1'. The zoomed-in view shows that the nodal lines from the two TPs intersect with two ANLs.

When carbon dimerization in CHC-1 [see the orange atoms in Fig. 7(b)] is removed, the structure becomes CHC-1' in Fig. 7(c). To see the effect of the de-dimerization, the contour map of CHC-1' is plotted in Fig. 19(f) for $k_y = 0$ in a $1 \times 1 \times 2$ supercell to match that of CHC-1. The map reveals a pair of

triple points at $k_z = \pm 0.07 \pi/2c'$ (where c' is the lattice constant of CHC-1'), which are connected by the $(-1, 0)$ nodal line. Interestingly, besides the nodal line along k_z , two additional nodal lines along k_x can be seen around $k_z = \pm 0.02 \pi/2c'$. Here, the structure has a 6-fold screw rotation symmetry. There are therefore 5 additional pairs of equivalent nodal lines on the two mirror planes $k_y = \pm\sqrt{3}k_x$ and on three glide planes $k_x = 0, \pm\sqrt{3}k_y$. The total number of nodal lines not crossing the TPs are therefore 12, as schematically illustrated in Fig. 19(c).

Constrained by the symmetry group and the time reversal symmetry for a spinless system, one obtains a 3×3 $\mathbf{k} \cdot \mathbf{p}$ model around the Γ point³²¹:

$$H(\mathbf{k}) = \begin{bmatrix} A_1 k_{\parallel}^2 + B_1 \cos k_z + C_1 & \alpha k_+ \sin k_z + \beta k_-^2 & Dk_- \\ \alpha k_- \sin k_z + \beta k_+^2 & A_1 k_{\parallel}^2 + B_1 \cos k_z + C_1 & -Dk_+ \\ Dk_+ & -Dk_- & A_2 k_{\parallel}^2 + B_2 \cos k_z + C_2 \end{bmatrix}, \quad (8)$$

where $k_{\pm} = k_x \pm ik_y$, $k_{\parallel}^2 = k_x^2 + k_y^2$, and $A_{1,2}$, $B_{1,2}$, $C_{1,2}$, D , α, β are real constants. When $\alpha = \beta = 0$, it describes the triple point phase. When $\alpha = 0$ and $\beta \neq 0$, it describes the triple points and nodal lines phase. Therefore, the effect of the βk_{\pm}^2 term is to generate additional nodal lines on the mirror/glide planes. While the effect of the $\alpha k_{\pm} \sin k_z$ term is splitting the trivial line in the triple point phase, as this term decreases the structural symmetry. When $\beta = 0$ and $\alpha \neq 0$, it describes a standard nexus-point phase. The nexus network is generated only in the case of $\alpha \neq 0$ and $\beta \neq 0$. This illustrates that the nexus network is a result of the interactions between the standard nexus point phase and additional nodal lines. Note that the $\mathbf{k} \cdot \mathbf{p}$ Hamiltonian above not only reproduces the nexus network in CHC-1, but can also be used to generate other nexus networks which may exist in other real materials as detailed in Ref. [321].

So far, various topological phases have been found in 3D carbon allotropes, from (Dirac, Weyl and triple) nodal points to nodal lines/rings/chains to nodal surfaces. We should also point out that topological phases in 3D carbon allotropes have also been discussed in the studies of Bernal graphite³⁴⁵, Mackey-Terrones crystal¹⁶³, body-centered orthorhombic C_{16} ⁴⁴, body-centered tetragonal C_{16} ⁴³ and m - C_8 ⁴⁷ (see Table 1).

4.5 Extension to boron and beyond

The topological classification of carbon allotropes different from the conventional topological materials is primarily originated from the negligible spin-orbit coupling in carbon materials. Generally speaking, materials consist of light elements should have the same topological classification³⁴⁶. For example, the Dirac points or nodal line also can be found in boron allotropes³⁴⁷⁻³⁵².

Very recently, Feng *et al.* discovered the Dirac fermion in β_{12} boron sheet with the aid of angle-resolved photoemission spectroscopy and first-principle calculations³⁵⁰. Chen *et al.* set out to determine whether a monolayer boron sheet with Dirac fermions was experimentally feasible, and they identified a new boron monolayer consisting of hexagon as well as rhombus stripes³⁴⁸. The boron monolayer, which has been called hr-sB, has an exceptional stability and unique Dirac fermions, as shown in Fig. 20(a). Dirac nodal lines and tilted semi-Dirac cones coexist around the E_F , and the Dirac points in the nodal lines are crossed by two linear bands corresponding to two 1D channels in the hexagon and rhombus stripes, respectively. The tilted semi-Dirac cones are present at the tilted axis and anisotropic band crossings, which produces a new kind of Dirac fermions. The unique electronic properties, as a result of the special bonding characteristics, indicate that this boron monolayer may be a good superconductor³⁴⁸.

By means of systematic first principles computations, Chen *et al.* also discovered another stable 3D boron allotrope, namely 3D- α' boron, which is a nodal-chain semimetal as shown in Fig. 20(b)³⁴⁷. In momentum space, six nodal lines and rings contact each other and form a novel spindle nodal chain [see Fig. 20(c)]. The band structure in Fig. 20(d) and PDOS in Fig. 20(e) indicate that the electronic properties of the 3D- α' boron are also dominated by π bonds, similar to the case in 3D graphene networks. This 3D- α' boron can be formed by stacking 2D wiggle α' boron sheets, which are also nodal-ring semimetals. In addition, our chemical bond analysis revealed that the topological properties of the 3D and 2D boron structures are related to the π bonds between boron atoms, although the bonding characteristics are qualitatively different from those in 2D and 3D carbon structures^{347,348}.

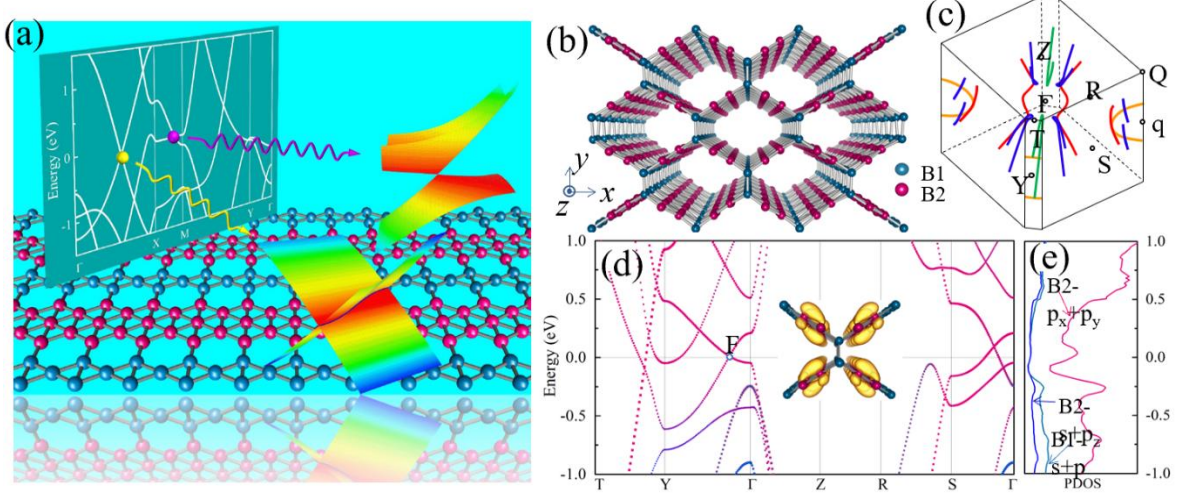


Figure 20. (a) A single layer boron sheet hr-sB possessing Dirac nodal line and tilted Dirac cone. (b) Atomic structure of a boron allotrope 3D- α' boron, which can be formed by stacking 2D wiggly α' boron sheets. (c) Nodal lines in the first BZ of 3D- α' boron. (d-e) Band structures and PDOS of 3D- α' boron, respectively. The inset in (d) shows a charge density for a state at point F.

V. Final remarks

(1) Before ending, we stress that in the above discussions, electron spin is treated as a dummy variable because of the negligibly small SOC strength. Then the fundamental time reversal operation (T) here satisfies $T^2 = 1$, contrasting with $T^2 = -1$ for the spin case³⁵³. As such, in terms of topological classifications, the nontrivial phases in light-elements materials would be fundamentally distinct from those in SOC systems.

(2) While most of the 3D carbon structures discussed here have not been experimentally synthesized thus far, except for the CHCs, we note that the advancement in MXene-derived carbon [see Fig. 21]¹⁴³ and MOF-derived carbon [see Fig. 22]^{142,354,355} may hold the key for the eventual experimental realization of 3D topological carbon materials, as such processes may maximally maintain the atomic structures of the carbon skeleton or its derivatives in an orderly fashion. This is especially encouraging given the fact that there are many thousands of MOFs and COFs available to explore. Even the variety of the MXene is considerable. On the flip side, the large variety also calls for a future theoretical investigation of the exotic topological properties of the MOF- and MXene-derived carbon networks and their potential applications.

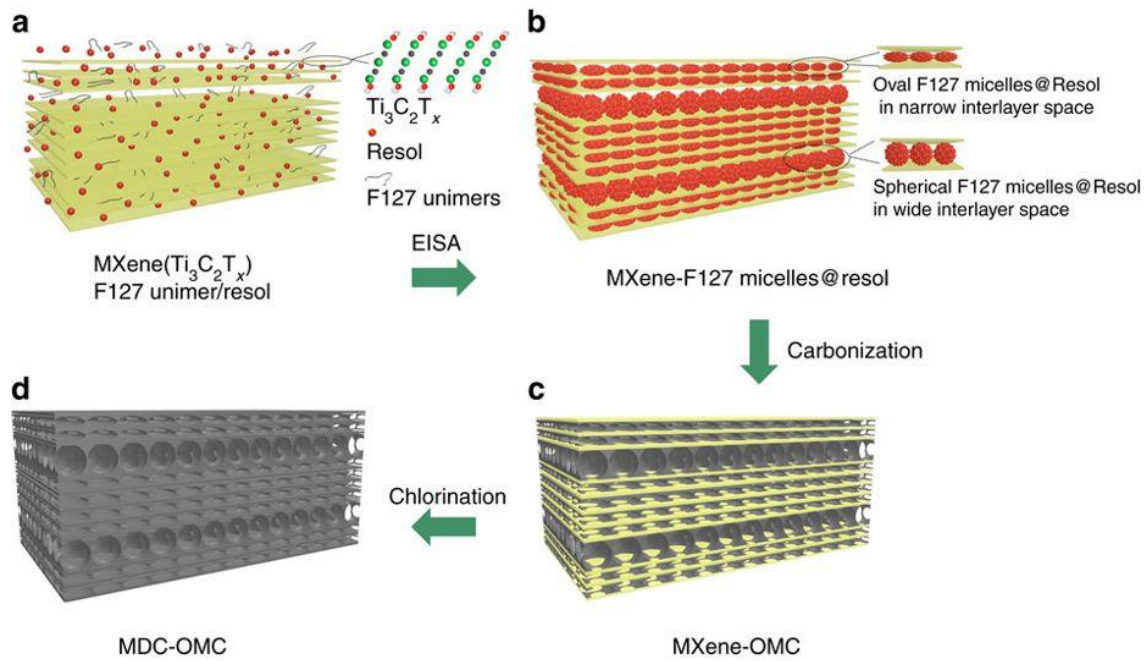


Figure 21. Preparation of the (a) MXene/F127 unimer/resol mixture, (b) MXene-F127 micelles@resol composite, (c) MXene-OMC composite and (d) MDC-OMC composite.

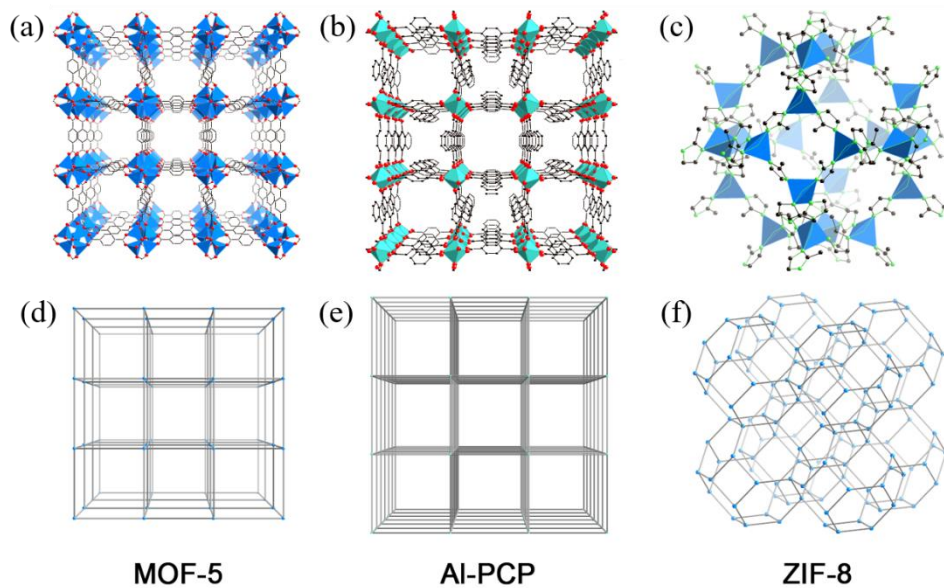


Figure 22. Crystal structures (a-c) and simplified framework structures (d-f) of MOF-5 ($Zn_4O(1,4\text{-benzenedicarboxylate})_3$; left), Al-PCP ($Al(OH)(1,4\text{-naphthalenedicarboxylate})$; middle), and ZIF-8 ($Zn(2\text{-methylimidazolate})_2$; right).

(3) We note the recent significant surge in the interest and study of twisted graphene³⁵⁶⁻³⁶⁴. In retrospect, twisted graphene shares the same orbital physics as the carbon networks elaborated on in this review article. In particular, both start with the non-trivial orbital topology that manifest as the Dirac cones of a single-layer graphene. However, twisting results in a (more complex) Moiré pattern

of the p_z orbitals (see Fig. 23) than what we have here. It has been speculated that in the twisted graphene bilayer a strong interlayer resonance leads to an in-plane localization and hence a flat band³⁶⁵⁻³⁶⁷. We, however, feel that the physics of the twisted graphene may resemble the flat band physics of monolayer carbon Kagome lattice discussed in Secs. 2.2 and 4.3, although the exact origin for the wavefunction phase cancellation may differ. Recently, it has been experimentally shown that Kagome lattice indeed form as a result of twisting of a silicene bilayer [see Fig. 24], in spite that the twist angle is considerably larger than what has been reported for the twisted graphene bilayer³⁶⁸.

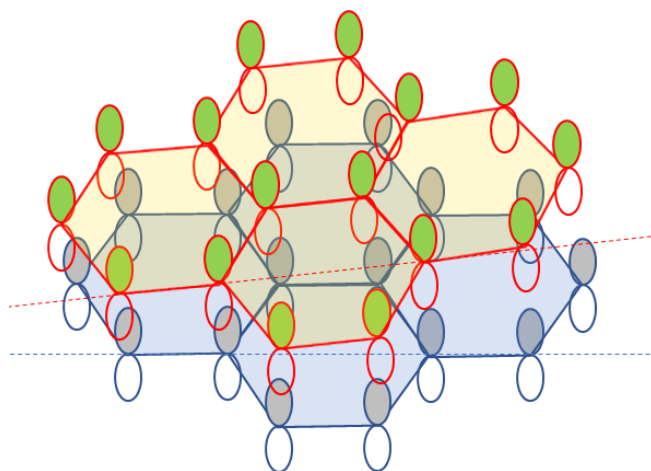


Figure 23. A schematic view of twist bilayer graphene.

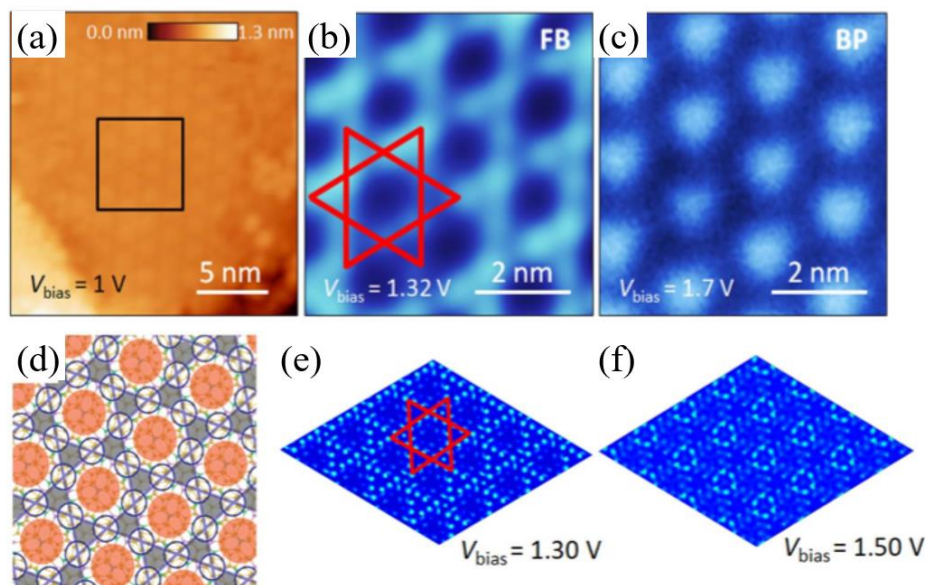


Figure 24. (a) STM image of large-scale Kagome lattice. (b and c) DOS mappings of the region enclosed by the black square in (a). (d) Structural model of an interlayer twist silicene multilayer. Two kinds of AA stacking sites are marked by red and black plates, respectively. (e and f) DFT simulation images.

(4) Besides the topological properties discussed here, which are also known as the first order, recently higher-order TIs has also attracted considerable interests. While the higher orders are classified by different Chern numbers from the first order, physically they represent an expansion of the gaped states at the expense of the gapless states. For example, for a 3D bulk, in the first order, the gapless states cover all the surfaces. In the second order, the gapless states only cover all the edges. On the other hand, in the third order, the gapless states cover only all the corners. For a 2D bulk, in contrast, the first order is featured by gapless edge states, while the second order is featured by gapless corner states. It has been proposed that some of the graphynes discussed earlier are in fact the first second-order TIs [see Fig. 25]. If this is true and since the materials are already been synthesized, they could be the first example of second-order TIs to be experimentally synthesized. Hence, not only the very first-order TI was born in a carbon material, i.e., the graphene, but the second-order TL was born also in a carbon material.

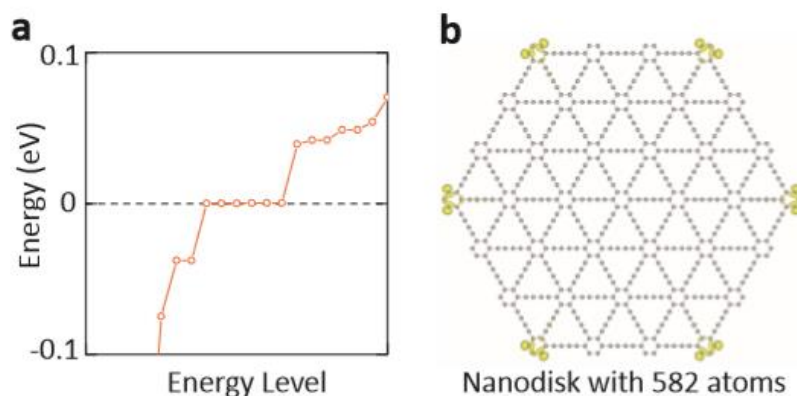


Figure 25. Corner states in graphdiyne. (a) Energy spectrum of the hexagonal-shaped GDY nanodisk shown in (b). The energy levels are plotted in ascending order. (b) also shows the charge distribution of the six zero energy modes, demonstrating that they are localized at corners.

(5) Last but not least, we would like to stress the vital importance of understanding the topological physics in carbon materials, not only because of the unique position of carbon in many technologically-important applications, but also because of its cleanest topological electronic states. Here, only one p orbital participates in the topologically nontrivial gapless states over a wide energy gap of almost 10 eV. In contrast in most of the known topological materials, not only the composition of the gapless states is more than one, but also topological trivial states often dominate over the energy spectrum near the Fermi level. No wonder their silent topological properties must wait for nearly 80 years after the

birth of quantum mechanics and 20 years after the quantum Hall effect to be uncovered. Hence, from the point of views of both applications and a thorough understanding of the band topology in condensed matter, we ought to fabricate 3D carbon networks in high quality and characterize them, and the time has come.

In summary, we have reviewed topological properties and topological phenomena in carbon structures. One can expect that other materials made of light elements possess similar exotic characteristics. In addition, for materials having a larger SOC, if they have the same topological class as the light-element structures in the absence of the SOC, the effects of the SOC may go beyond just opening band gaps at the band crossings possibly leading to new topological phases unexplored so far. While the review has been focused on topological phases of carbon materials, we can expect that the topological phases will influence other physical properties.

Topological Classification	Material candidates
2D Dirac (Weyl) semimetal	graphene, S/D/E-graphene, ph-graphene phagraphene, graphyne family, Kagome graphene
3D nodal line semimetal	IGN, Bco-C16, Bct-C16, m-C8, Mackey-Terrones crystal, Bernal graphite
novel TMs	T/Q/HGN(n, n), Weyl-surface semimetal ; Pentagon Carbon, triply-degenerate and Weyl-loop metal

Table 1. The topological classification in carbon materials.

ACKNOWLEDGEMENTS

YPC acknowledges support by the National Natural Science Foundation of China (No. 11874314). MLC acknowledges support from the National Science Foundation Grant No. DMR-1508412 and from the Theory of Materials Program at the Lawrence Berkeley National Lab funded by the Director, Office

of Science and Office of Basic Energy Sciences, Materials Sciences and Engineering Division, U.S. Department of Energy under Contract No. DE-AC02-05CH11231. SBZ acknowledges support by U.S. Department of Energy under Grant No. DE-SC0002623.

References

- 1 Falcao, E. H. & Wudl, F. Carbon allotropes: beyond graphite and diamond. *Journal of Chemical Technology & Biotechnology: International Research in Process, Environmental & Clean Technology* **82**, 524-531 (2007).
- 2 Zhang, Q., Huang, J. Q., Qian, W. Z., Zhang, Y. Y. & Wei, F. The road for nanomaterials industry: A review of carbon nanotube production, post - treatment, and bulk applications for composites and energy storage. *Small* **9**, 1237-1265 (2013).
- 3 Zhang, R.-S. & Jiang, J.-W. The art of designing carbon allotropes. *Frontiers of Physics* **14**, 13401 (2019).
- 4 Balch, A. L. & Winkler, K. Two-component polymeric materials of fullerenes and the transition metal complexes: A bridge between metal–organic frameworks and conducting polymers. *Chemical reviews* **116**, 3812-3882 (2016).
- 5 Terrones, M. *et al.* Graphene and graphite nanoribbons: Morphology, properties, synthesis, defects and applications. *Nano today* **5**, 351-372 (2010).
- 6 Allen, M. J., Tung, V. C. & Kaner, R. B. Honeycomb carbon: a review of graphene. *Chemical reviews* **110**, 132-145 (2009).
- 7 Yu, L., Shearer, C. & Shapter, J. Recent development of carbon nanotube transparent conductive films. *Chemical reviews* **116**, 13413-13453 (2016).
- 8 Bonaccorso, F. *et al.* Graphene, related two-dimensional crystals, and hybrid systems for energy conversion and storage. *Science* **347**, 1246501 (2015).
- 9 Geim, A. K. Graphene: status and prospects. *science* **324**, 1530-1534 (2009).
- 10 Belenkov, E. A. & Greshnyakov, V. A. Classification schemes for carbon phases and nanostructures. *New Carbon Materials* **28**, 273-282 (2013).
- 11 Neto, A. C., Guinea, F., Peres, N. M., Novoselov, K. S. & Geim, A. K. The electronic properties of graphene. *Reviews of modern physics* **81**, 109 (2009).
- 12 Katsnelson, M. I. Graphene: carbon in two dimensions. *Materials today* **10**, 20-27 (2007).
- 13 Balandin, A. A. Thermal properties of graphene and nanostructured carbon materials. *Nature materials* **10**, 569 (2011).
- 14 Manna, K., Sun, Y., Muechler, L., Kübler, J. & Felser, C. Heusler, Weyl and Berry. *Nature Reviews Materials*, 1 (2018).
- 15 Yu, R., Fang, Z., Dai, X. & Weng, H. Topological nodal line semimetals predicted from first-principles calculations. *Frontiers of Physics* **12**, 127202 (2017).
- 16 Tokura, Y., Yasuda, K. & Tsukazaki, A. Magnetic topological insulators. *Nature Reviews Physics*,

-
- 1 (2019).
 - 17 Hasan, M. Z. & Kane, C. L. Colloquium: topological insulators. *Reviews of modern physics* **82**, 3045 (2010).
 - 18 Rachel, S. Interacting topological insulators: a review. *Reports on Progress in Physics* **81**, 116501 (2018).
 - 19 Ren, Y., Qiao, Z. & Niu, Q. Topological phases in two-dimensional materials: a review. *Reports on Progress in Physics* **79**, 066501 (2016).
 - 20 Qi, X.-L. & Zhang, S.-C. Topological insulators and superconductors. *Reviews of Modern Physics* **83**, 1057 (2011).
 - 21 Chiu, C.-K., Teo, J. C., Schnyder, A. P. & Ryu, S. Classification of topological quantum matter with symmetries. *Reviews of Modern Physics* **88**, 035005 (2016).
 - 22 Armitage, N., Mele, E. & Vishwanath, A. Weyl and Dirac semimetals in three-dimensional solids. *Reviews of Modern Physics* **90**, 015001 (2018).
 - 23 Gao, H., Venderbos, J. W., Kim, Y. & Rappe, A. M. Topological Semimetals from first-principles. *arXiv preprint arXiv:1810.08186* (2018).
 - 24 Qi, X.-L., Li, R., Zang, J. & Zhang, S.-C. Inducing a magnetic monopole with topological surface states. *Science* **323**, 1184-1187 (2009).
 - 25 Alicea, J. New directions in the pursuit of Majorana fermions in solid state systems. *Reports on progress in physics* **75**, 076501 (2012).
 - 26 Yan, B. & Zhang, S.-C. Topological materials. *Reports on Progress in Physics* **75**, 096501 (2012).
 - 27 Ando, Y. Topological insulator materials. *Journal of the Physical Society of Japan* **82**, 102001 (2013).
 - 28 Bansil, A., Lin, H. & Das, T. Colloquium: Topological band theory. *Reviews of Modern Physics* **88**, 021004 (2016).
 - 29 Yan, B. & Felser, C. Topological materials: Weyl semimetals. *Annual Review of Condensed Matter Physics* **8**, 337-354 (2017).
 - 30 Klemenz, S., Lei, S. & Schoop, L. M. Topological Semimetals in Square-Net Materials. *Annual Review of Materials Research* (2019).
 - 31 Kane, C. L. & Mele, E. J. Z₂ topological order and the quantum spin Hall effect. *Physical review letters* **95**, 146802 (2005).
 - 32 Novoselov, K. S. *et al.* Two-dimensional gas of massless Dirac fermions in graphene. *nature* **438**, 197 (2005).
 - 33 Park, C.-H., Yang, L., Son, Y.-W., Cohen, M. L. & Louie, S. G. Anisotropic behaviours of massless Dirac fermions in graphene under periodic potentials. *Nature Physics* **4**, 213 (2008).
 - 34 Levin, M. & Stern, A. Fractional topological insulators. *Physical review letters* **103**, 196803 (2009).
 - 35 Analytis, J. G. *et al.* Two-dimensional surface state in the quantum limit of a topological insulator. *Nature Physics* **6**, 960 (2010).
 - 36 Chen, Y. *et al.* Nanostructured carbon allotropes with Weyl-like loops and points. *Nano letters* **15**, 6974-6978 (2015).
 - 37 Tan, L. Z., Park, C.-H. & Louie, S. G. New dirac fermions in periodically modulated bilayer graphene. *Nano letters* **11**, 2596-2600 (2011).

-
- 38 Wang, Z. *et al.* Phagraphene: a low-energy graphene allotrope composed of 5–6–7 carbon rings with distorted dirac cones. *Nano letters* **15**, 6182-6186 (2015).
- 39 Park, M., Kim, Y. & Lee, H. Design of 2D massless Dirac fermion systems and quantum spin Hall insulators based on sp–sp² carbon sheets. *npj Computational Materials* **4**, 54 (2018).
- 40 Yang, D., Si, M., Zhang, G. & Xue, D. Crystal momentum-dependent anisotropy of the Dirac cone in the rectangular carbon allotropes. *EPL (Europhysics Letters)* **107**, 20003 (2014).
- 41 Zhang, L. *et al.* Highly anisotropic Dirac fermions in square graphynes. *The journal of physical chemistry letters* **6**, 2959-2962 (2015).
- 42 Wang, J.-T., Chen, C. & Kawazoe, Y. Topological nodal line semimetal in an orthorhombic graphene network structure. *Physical Review B* **97**, 245147 (2018).
- 43 Cheng, Y. *et al.* Body - Centered Tetragonal C16: A Novel Topological Node - Line Semimetallic Carbon Composed of Tetrarings. *small* **13**, 1602894 (2017).
- 44 Wang, J.-T. *et al.* Body-centered orthorhombic c 16: A novel topological node-line semimetal. *Physical review letters* **116**, 195501 (2016).
- 45 Liu, J., Li, X., Wang, Q., Kawazoe, Y. & Jena, P. A new 3D Dirac nodal-line semi-metallic graphene monolith for lithium ion battery anode materials. *Journal of Materials Chemistry A* **6**, 13816-13824 (2018).
- 46 Feng, X. *et al.* Monoclinic C16: sp²-sp³ hybridized nodal-line semimetal protected by PT-symmetry. *Carbon* **127**, 527-532 (2018).
- 47 Sung, H.-J., Kim, S., Lee, I.-H. & Chang, K. J. Semimetallic carbon allotrope with a topological nodal line in mixed sp-sp² 2-sp³ bonding networks. *NPG Asia Materials* **9**, e361 (2017).
- 48 Lin, Y., Zhao, Z., Strobel, T. A. & Cohen, R. Interpenetrating graphene networks: Three-dimensional node-line semimetals with massive negative linear compressibilities. *Physical Review B* **94**, 245422 (2016).
- 49 Zhong, C. *et al.* Two-dimensional honeycomb borophene oxide: strong anisotropy and nodal loop transformation. *Nanoscale* **11**, 2468-2475 (2019).
- 50 Qie, Y., Liu, J., Wang, S., Sun, Q. & Jena, P. Tetragonal C 24: a topological nodal-surface semimetal with potential as an anode material for sodium ion batteries. *Journal of Materials Chemistry A* **7**, 5733-5739 (2019).
- 51 Zhong, C. *et al.* Towards three-dimensional Weyl-surface semimetals in graphene networks. *Nanoscale* **8**, 7232-7239 (2016).
- 52 Gao, Y. *et al.* Electron and phonon properties and gas storage in carbon honeycombs. *Nanoscale* **8**, 12863-12868 (2016).
- 53 Su, W. P., Schrieffer, J. & Heeger, A. J. Solitons in polyacetylene. *Physical review letters* **42**, 1698 (1979).
- 54 Iijima, S. Helical microtubules of graphitic carbon. *nature* **354**, 56 (1991).
- 55 Terrones, H. *et al.* New metallic allotropes of planar and tubular carbon. *Physical review letters* **84**, 1716 (2000).
- 56 Liu, A. Y., Cohen, M. L., Hass, K. & Tamor, M. Structural properties of a three-dimensional all-sp² phase of carbon. *Physical Review B* **43**, 6742 (1991).
- 57 Chiang, C. K. *et al.* Electrical conductivity in doped polyacetylene. *Physical review letters* **39**, 1098 (1977).

-
- 58 Shirakawa, H. Nobel lecture: the discovery of polyacetylene film—the dawning of an era of conducting polymers. *Reviews of Modern Physics* **73**, 713 (2001).
- 59 Guo, X., Lee, W. H., Alvarez, N., Shanov, V. N. & Heineman, W. R. Detection of trace zinc by an electrochemical microsensor based on carbon nanotube threads. *Electroanalysis* **25**, 1599-1604 (2013).
- 60 Tang, Y. *et al.* Synthesis and characterization of amorphous carbon nanowires. *Applied physics letters* **75**, 2921-2923 (1999).
- 61 Li, D. & Kaner, R. B. Graphene-based materials. *Science* **320**, 1170-1171 (2008).
- 62 Meyer, J. C. *et al.* The structure of suspended graphene sheets. *Nature* **446**, 60 (2007).
- 63 Kim, K. S. *et al.* Large-scale pattern growth of graphene films for stretchable transparent electrodes. *nature* **457**, 706 (2009).
- 64 Novoselov, K. S. *et al.* Room-temperature quantum Hall effect in graphene. *Science* **315**, 1379-1379 (2007).
- 65 Du, X., Skachko, I., Barker, A. & Andrei, E. Y. Approaching ballistic transport in suspended graphene. *Nature nanotechnology* **3**, 491 (2008).
- 66 Zhu, Y. *et al.* Carbon-based supercapacitors produced by activation of graphene. *science* **332**, 1537-1541 (2011).
- 67 Hwang, E., Adam, S. & Sarma, S. D. Carrier transport in two-dimensional graphene layers. *Physical review letters* **98**, 186806 (2007).
- 68 Liu, Y. & Chen, X. Mechanical properties of nanoporous graphene membrane. *Journal of Applied Physics* **115**, 034303 (2014).
- 69 Balandin, A. A. *et al.* Superior thermal conductivity of single-layer graphene. *Nano letters* **8**, 902-907 (2008).
- 70 Novoselov, K. S. *et al.* Electric field effect in atomically thin carbon films. *science* **306**, 666-669 (2004).
- 71 Hernandez, Y. *et al.* High-yield production of graphene by liquid-phase exfoliation of graphite. *Nature nanotechnology* **3**, 563 (2008).
- 72 Chia, J. S. Y. *et al.* A novel one step synthesis of graphene via sonochemical-assisted solvent exfoliation approach for electrochemical sensing application. *Chemical Engineering Journal* **249**, 270-278 (2014).
- 73 Huang, N., Lim, H., Chia, C. H., Yarmo, M. A. & Muhamad, M. Simple room-temperature preparation of high-yield large-area graphene oxide. *International journal of nanomedicine* **6**, 3443 (2011).
- 74 Chen, W., Yan, L. & Bangal, P. R. Preparation of graphene by the rapid and mild thermal reduction of graphene oxide induced by microwaves. *Carbon* **48**, 1146-1152 (2010).
- 75 Rostrup-Nielsen, J. & Trimm, D. L. Mechanisms of carbon formation on nickel-containing catalysts. *Journal of Catalysis* **48**, 155-165 (1977).
- 76 Chae, S. J. *et al.* Synthesis of large - area graphene layers on poly - nickel substrate by chemical vapor deposition: wrinkle formation. *Advanced materials* **21**, 2328-2333 (2009).
- 77 Al-Temimy, A., Riedl, C. & Starke, U. Low temperature growth of epitaxial graphene on SiC induced by carbon evaporation. *Applied Physics Letters* **95**, 231907 (2009).
- 78 Chen, W. & Yan, L. Preparation of graphene by a low-temperature thermal reduction at atmosphere pressure. *Nanoscale* **2**, 559-563 (2010).

-
- 79 Reina, A. *et al.* Large area, few-layer graphene films on arbitrary substrates by chemical vapor deposition. *Nano letters* **9**, 30-35 (2008).
- 80 Gomez De Arco, L. *et al.* Continuous, highly flexible, and transparent graphene films by chemical vapor deposition for organic photovoltaics. *ACS nano* **4**, 2865-2873 (2010).
- 81 Crespi, V. H., Benedict, L. X., Cohen, M. L. & Louie, S. G. Prediction of a pure-carbon planar covalent metal. *Physical Review B* **53**, R13303 (1996).
- 82 Schmidt, O. G. & Eberl, K. Nanotechnology: Thin solid films roll up into nanotubes. *Nature* **410**, 168 (2001).
- 83 Zhang, X. *et al.* Synthesis and characterization of a graphene–C60 hybrid material. *Carbon* **47**, 334-337 (2009).
- 84 Mandal, B., Sarkar, S., Pramanik, A. & Sarkar, P. Theoretical prediction of a new two-dimensional carbon allotrope and NDR behaviour of its one-dimensional derivatives. *Physical Chemistry Chemical Physics* **15**, 21001-21006 (2013).
- 85 Charlier, J.-C., Gonze, X. & Michenaud, J.-P. First-principles study of the electronic properties of graphite. *Physical Review B* **43**, 4579 (1991).
- 86 Dresselhaus, M., Dresselhaus, G. & Saito, R. Physics of carbon nanotubes. *Carbon* **33**, 883-891 (1995).
- 87 Barone, V., Hod, O. & Scuseria, G. E. Electronic structure and stability of semiconducting graphene nanoribbons. *Nano letters* **6**, 2748-2754 (2006).
- 88 Yang, X. *et al.* Two-dimensional graphene nanoribbons. *Journal of the American Chemical Society* **130**, 4216-4217 (2008).
- 89 Brey, L. & Fertig, H. Electronic states of graphene nanoribbons studied with the Dirac equation. *Physical Review B* **73**, 235411 (2006).
- 90 Zheng, H., Wang, Z., Luo, T., Shi, Q. & Chen, J. Analytical study of electronic structure in armchair graphene nanoribbons. *Physical Review B* **75**, 165414 (2007).
- 91 Jaskólski, W., Ayuela, A., Pelc, M., Santos, H. & Chico, L. Edge states and flat bands in graphene nanoribbons with arbitrary geometries. *Physical Review B* **83**, 235424 (2011).
- 92 Liao, W., Zhou, G. & Xi, F. (AIP, 2008).
- 93 Hu, J., Ruan, X. & Chen, Y. P. Thermal conductivity and thermal rectification in graphene nanoribbons: a molecular dynamics study. *Nano letters* **9**, 2730-2735 (2009).
- 94 Baringhaus, J. *et al.* Exceptional ballistic transport in epitaxial graphene nanoribbons. *Nature* **506**, 349 (2014).
- 95 Bai, J. *et al.* Very large magnetoresistance in graphene nanoribbons. *Nature nanotechnology* **5**, 655 (2010).
- 96 Koch, M., Ample, F., Joachim, C. & Grill, L. Voltage-dependent conductance of a single graphene nanoribbon. *Nature nanotechnology* **7**, 713 (2012).
- 97 Malko, D., Neiss, C., Vines, F. & Görling, A. Competition for graphene: graphynes with direction-dependent dirac cones. *Physical review letters* **108**, 086804 (2012).
- 98 Puigdollers, A. R., Alonso, G. & Gamallo, P. First-principles study of structural, elastic and electronic properties of α -, β - and γ -graphyne. *Carbon* **96**, 879-887 (2016).
- 99 Kim, H., Kim, Y., Kim, J. & Kim, W. Y. Computational searching for new stable graphyne structures and their electronic properties. *Carbon* **98**, 404-410 (2016).

-
- 100 Perkgöz, N. K. & Sevik, C. Vibrational and thermodynamic properties of α -, β -, γ -, and 6, 6, 12-graphyne structures. *Nanotechnology* **25**, 185701 (2014).
- 101 Yin, W.-J. *et al.* R-graphyne: a new two-dimensional carbon allotrope with versatile Dirac-like point in nanoribbons. *Journal of Materials Chemistry A* **1**, 5341-5346 (2013).
- 102 Nulakani, N. V. R. & Subramanian, V. A theoretical study on the design, structure, and electronic properties of novel forms of graphynes. *The Journal of Physical Chemistry C* **120**, 15153-15161 (2016).
- 103 Malko, D., Neiss, C. & Görling, A. Two-dimensional materials with Dirac cones: Graphynes containing heteroatoms. *Physical Review B* **86**, 045443 (2012).
- 104 Ni, Y. *et al.* The transport properties and new device design: the case of 6, 6, 12-graphyne nanoribbons. *Nanoscale* **5**, 4468-4475 (2013).
- 105 Ding, H., Bai, H. & Huang, Y. Electronic properties and carrier mobilities of 6, 6, 12-graphyne nanoribbons. *AIP Advances* **5**, 077153 (2015).
- 106 Shabalyn, I. L. in *Ultra-high temperature materials I* 7-235 (Springer, 2014).
- 107 Kang, J., Li, J., Wu, F., Li, S.-S. & Xia, J.-B. Elastic, electronic, and optical properties of two-dimensional graphyne sheet. *The Journal of Physical Chemistry C* **115**, 20466-20470 (2011).
- 108 Kang, B., Liu, H. & Lee, J. Y. Oxygen adsorption on single layer graphyne: a DFT study. *Physical Chemistry Chemical Physics* **16**, 974-980 (2014).
- 109 Mortazavi, B., Shahrokhi, M., Rabczuk, T. & Pereira, L. F. C. Electronic, optical and thermal properties of highly stretchable 2D carbon Ene-yne graphyne. *Carbon* **123**, 344-353 (2017).
- 110 Ouyang, T. *et al.* Thermal transport in graphyne nanoribbons. *Physical Review B* **85**, 235436 (2012).
- 111 Ram, B. & Mizuseki, H. Tetrahexcarbon: A two-dimensional allotrope of carbon. *Carbon* **137**, 266-273 (2018).
- 112 Karaush, N. N., Baryshnikov, G. V. & Minaev, B. F. DFT characterization of a new possible graphene allotrope. *Chemical Physics Letters* **612**, 229-233 (2014).
- 113 Wang, X.-Q., Li, H.-D. & Wang, J.-T. Prediction of a new two-dimensional metallic carbon allotrope. *Physical Chemistry Chemical Physics* **15**, 2024-2030 (2013).
- 114 Yi, W.-c., Liu, W., Botana, J., Liu, J.-y. & Miao, M.-s. Microporosity as a new property control factor in graphene-like 2D allotropes. *Journal of Materials Chemistry A* **6**, 10348-10353 (2018).
- 115 Chen, Y. *et al.* Ferromagnetism and Wigner crystallization in kagome graphene and related structures. *Physical Review B* **98**, 035135 (2018).
- 116 Liu, Y., Wang, G., Huang, Q., Guo, L. & Chen, X. Structural and electronic properties of T graphene: a two-dimensional carbon allotrope with tetrarings. *Physical review letters* **108**, 225505 (2012).
- 117 Cohen, M. L. Calculation of bulk moduli of diamond and zinc-blende solids. *Physical Review B* **32**, 7988 (1985).
- 118 Bernal, J. D. The structure of graphite. *Proceedings of the Royal Society of London. Series A, Containing Papers of a Mathematical and Physical Character* **106**, 749-773 (1924).
- 119 Ramdas, A., Rodriguez, S., Grimsditch, M., Anthony, T. & Banholzer, W. Effect of isotopic constitution of diamond on its elastic constants: C 13 diamond, the hardest known material. *Physical review letters* **71**, 189 (1993).
- 120 Li, Z., Gao, F. & Xu, Z. Strength, hardness, and lattice vibrations of Z-carbon and W-carbon: first-

-
- principles calculations. *Physical Review B* **85**, 144115 (2012).
- 121 Selli, D., Baburin, I. A., Martoňák, R. & Leoni, S. Superhard sp³ carbon allotropes with odd and even ring topologies. *Physical Review B* **84**, 161411 (2011).
- 122 Wang, J.-T., Chen, C. & Kawazoe, Y. Low-Temperature Phase Transformation from Graphite to sp³ Orthorhombic Carbon. *Physical Review Letters* **106**, 075501 (2011).
- 123 Zhao, Z. *et al.* Novel superhard carbon: C-centered orthorhombic C₈. *Physical review letters* **107**, 215502 (2011).
- 124 Umemoto, K., Wentzcovitch, R. M., Saito, S. & Miyake, T. Body-Centered Tetragonal C₄: A Viable sp³ Carbon Allotrope. *Physical review letters* **104**, 125504 (2010).
- 125 Chen, X.-Q., Niu, H., Franchini, C., Li, D. & Li, Y. Hardness of T-carbon: Density functional theory calculations. *Physical Review B* **84**, 121405 (2011).
- 126 Krainyukova, N. V. Capturing gases in carbon honeycomb. *Journal of Low Temperature Physics* **187**, 90-104 (2017).
- 127 Hu, M. *et al.* Low-energy 3D sp² carbons with versatile properties beyond graphite and graphene. *Dalton Transactions* **47**, 6233-6239 (2018).
- 128 Fthenakis, Z. G. Are the experimentally observed 3-dimensional carbon honeycombs all-sp² structures? The dangling p-orbital instability. *RSC Advances* **7**, 9790-9794 (2017).
- 129 Chen, Y. *et al.* Carbon kagome lattice and orbital-frustration-induced metal-insulator transition for optoelectronics. *Physical review letters* **113**, 085501 (2014).
- 130 Wang, J.-T., Nie, S., Weng, H., Kawazoe, Y. & Chen, C. Topological nodal-net semimetal in a graphene network structure. *Physical review letters* **120**, 026402 (2018).
- 131 Krainyukova, N. V. & Zubarev, E. N. Carbon honeycomb high capacity storage for gaseous and liquid species. *Physical review letters* **116**, 055501 (2016).
- 132 Hu, M. *et al.* Compressed glassy carbon: An ultrastrong and elastic interpenetrating graphene network. *Science advances* **3**, e1603213 (2017).
- 133 Sharma, S. Glassy Carbon: A Promising Material for Micro-and Nanomanufacturing. *Materials* **11**, 1857 (2018).
- 134 Wei, Q., Zhang, Q., Yan, H., Zhang, M. & Wei, B. A new tetragonal superhard metallic carbon allotrope. *Journal of Alloys and Compounds* **769**, 347-352 (2018).
- 135 Liu, Y., Jiang, X., Fu, J. & Zhao, J. New metallic carbon: Three dimensionally carbon allotropes comprising ultrathin diamond nanostripes. *Carbon* **126**, 601-610 (2018).
- 136 Li, Z. *et al.* Superhard superstrong carbon clathrate. *Carbon* **105**, 151-155 (2016).
- 137 Wei, Q. *et al.* A new superhard carbon allotrope: Orthorhombic C₂₀. *Physics Letters A* **382**, 1685-1689 (2018).
- 138 Pan, Y. *et al.* A superhard sp³ microporous carbon with direct bandgap. *Chemical Physics Letters* **689**, 68-73 (2017).
- 139 Liu, J., Zhao, T., Zhang, S. & Wang, Q. A new metallic carbon allotrope with high stability and potential for lithium ion battery anode material. *Nano energy* **38**, 263-270 (2017).
- 140 Wu, X. *et al.* Superhard three-dimensional carbon with metallic conductivity. *Carbon* **123**, 311-317 (2017).
- 141 Pan, Y. *et al.* Multithreaded conductive carbon: 1D conduction in 3D carbon. *Carbon* **115**, 584-588 (2017).

-
- 142 Chaikittisilp, W., Ariga, K. & Yamauchi, Y. A new family of carbon materials: synthesis of MOF-derived nanoporous carbons and their promising applications. *Journal of Materials Chemistry A* **1**, 14-19 (2013).
- 143 Wang, J. *et al.* Hierarchical porous carbons with layer-by-layer motif architectures from confined soft-template self-assembly in layered materials. *Nature communications* **8**, 15717 (2017).
- 144 Li, M., Zhang, X. & Zhao, Y. Superdense tI12 carbon: Unexpectedly high elastic moduli but low ideal strength. *Physics Letters A* **382**, 3125-3130 (2018).
- 145 Cui, H.-J. *et al.* The geometric and electronic transitions in body-centered-tetragonal C8: A first principle study. *Carbon* **120**, 89-94 (2017).
- 146 Cheng, C., Lv, Z.-L., Cheng, Y., Chen, X.-R. & Cai, L.-C. A possible superhard orthorhombic carbon. *Diamond and Related Materials* **43**, 49-54 (2014).
- 147 Pang, D.-D. *et al.* Properties of a predicted tetragonal carbon allotrope: First principles study. *Diamond and Related Materials* **82**, 50-55 (2018).
- 148 He, C. *et al.* New superhard carbon phases between graphite and diamond. *Solid State Communications* **152**, 1560-1563 (2012).
- 149 Kim, B. G., Sim, H. & Park, J. C4 Carbon allotropes with triple-bonds predicted by first-principles calculations. *Solid State Communications* **169**, 50-56 (2013).
- 150 Nulakani, N. V. R. & Subramanian, V. Superprismane: A porous carbon allotrope. *Chemical Physics Letters* **715**, 29-33 (2019).
- 151 Lv, Z.-L., Cui, H.-L., Wang, H., Li, X.-H. & Ji, G.-F. Theoretical study of the elasticity, ideal strength and thermal conductivity of a pure sp² carbon. *Diamond and Related Materials* **71**, 73-78 (2017).
- 152 Hu, M. *et al.* Three dimensional graphdiyne polymers with tunable band gaps. *Carbon* **91**, 518-526 (2015).
- 153 Bu, H., Zhao, M., Wang, A. & Wang, X. First-principles prediction of the transition from graphdiyne to a superlattice of carbon nanotubes and graphene nanoribbons. *Carbon* **65**, 341-348 (2013).
- 154 Gao, X. & Shen, X. Face-to-face crosslinking of graphdiyne and related carbon sheets toward integrated graphene nanoribbon arrays. *Carbon* **125**, 536-543 (2017).
- 155 Zhang, Z. *et al.* Nanomechanics of carbon honeycomb cellular structures. *Carbon* **113**, 26-32 (2017).
- 156 Costa, D. G., Henrique, F. J., Oliveira, F. L., Capaz, R. B. & Esteves, P. M. n-Diamondynes: Expanding the family of carbon allotropes. *Carbon* **136**, 337-344 (2018).
- 157 Li, X. & Xing, M. A reinvestigation of a superhard phase Cm-carbon. *Computational Materials Science* **143**, 32-42 (2018).
- 158 Bai, Y. *et al.* First-principles investigation in the Raman and infrared spectra of sp³ carbon allotropes. *Carbon* **78**, 70-78 (2014).
- 159 He, C. & Zhong, J. M585, a low energy superhard monoclinic carbon phase. *Solid State Communications* **181**, 24-27 (2014).
- 160 Fan, D., Lu, S., Golov, A. A., Kabanov, A. A. & Hu, X. D-carbon: Ab initio study of a novel carbon allotrope. *The Journal of chemical physics* **149**, 114702 (2018).
- 161 Kuc, A. & Seifert, G. Hexagon-preserving carbon foams: Properties of hypothetical carbon

-
- allotropes. *Physical Review B* **74**, 214104 (2006).
- 162 Yang, X. *et al.* Novel Superhard s p³ Carbon Allotrope from Cold-Compressed C₇₀ Peapods. *Physical review letters* **118**, 245701 (2017).
- 163 Weng, H. *et al.* Topological node-line semimetal in three-dimensional graphene networks. *Physical Review B* **92**, 045108 (2015).
- 164 Fu, L. & Kane, C. L. Topological insulators with inversion symmetry. *Physical Review B* **76**, 045302 (2007).
- 165 Burkov, A. Topological semimetals. *Nature materials* **15**, 1145 (2016).
- 166 Samarth, N. Quantum materials discovery from a synthesis perspective. *Nature materials* **16**, 1068 (2017).
- 167 Feng, W. & Yao, Y. Three-dimensional topological insulators: A review on host materials. *Science China Physics, Mechanics and Astronomy* **55**, 2199-2212 (2012).
- 168 Weng, H., Dai, X. & Fang, Z. Topological semimetals predicted from first-principles calculations. *Journal of Physics: Condensed Matter* **28**, 303001 (2016).
- 169 Yang, S. A. in *Spin*. 1640003 (World Scientific).
- 170 Lu, L., Joannopoulos, J. D. & Soljačić, M. Topological photonics. *Nature Photonics* **8**, 821 (2014).
- 171 Barik, R. K., Shinde, R. & Singh, A. K. Multiple triple-point fermions in Heusler compounds. *Journal of Physics: Condensed Matter* **30**, 375702 (2018).
- 172 Fang, C., Weng, H., Dai, X. & Fang, Z. Topological nodal line semimetals. *Chinese Physics B* **25**, 117106 (2016).
- 173 Türker, O. & Moroz, S. Weyl nodal surfaces. *Physical Review B* **97**, 075120 (2018).
- 174 Lu, L. *et al.* Experimental observation of Weyl points. *Science* **349**, 622-624 (2015).
- 175 Liu, Z. *et al.* A stable three-dimensional topological Dirac semimetal Cd₃As₂. *Nature materials* **13**, 677 (2014).
- 176 Liu, Z. *et al.* Discovery of a three-dimensional topological Dirac semimetal, Na₃Bi. *Science* **343**, 864-867 (2014).
- 177 Young, S. M. *et al.* Dirac semimetal in three dimensions. *Physical review letters* **108**, 140405 (2012).
- 178 Yang, H. *et al.* Prediction of triple point fermions in simple half-Heusler topological insulators. *Physical review letters* **119**, 136401 (2017).
- 179 Xie, Y., Cai, J., Kim, J., Chang, P.-Y. & Chen, Y. Hopf-chain networks evolved from triple points. *Physical Review B* **99**, 165147 (2019).
- 180 Zhu, Z., Winkler, G. W., Wu, Q., Li, J. & Soluyanov, A. A. Triple point topological metals. *Physical Review X* **6**, 031003 (2016).
- 181 Soluyanov, A. A. *et al.* Type-ii weyl semimetals. *Nature* **527**, 495 (2015).
- 182 Xiao, M., Lin, Q. & Fan, S. Hyperbolic Weyl point in reciprocal chiral metamaterials. *Physical review letters* **117**, 057401 (2016).
- 183 Bradlyn, B. *et al.* Beyond Dirac and Weyl fermions: Unconventional quasiparticles in conventional crystals. *Science* **353**, aaf5037 (2016).
- 184 Bian, G. *et al.* Topological nodal-line fermions in spin-orbit metal PbTaSe₂. *Nature communications* **7**, 10556 (2016).
- 185 Huang, H., Liu, J., Vanderbilt, D. & Duan, W. Topological nodal-line semimetals in alkaline-earth

-
- stannides, germanides, and silicides. *Physical Review B* **93**, 201114 (2016).
- 186 Xu, Q., Yu, R., Fang, Z., Dai, X. & Weng, H. Topological nodal line semimetals in the CaP 3 family of materials. *Physical Review B* **95**, 045136 (2017).
- 187 Li, K., Li, C., Hu, J., Li, Y. & Fang, C. Dirac and nodal line magnons in three-dimensional antiferromagnets. *Physical review letters* **119**, 247202 (2017).
- 188 Yan, Z. & Wang, Z. Floquet multi-Weyl points in crossing-nodal-line semimetals. *Physical Review B* **96**, 041206 (2017).
- 189 Zhang, X., Jin, L., Dai, X. & Liu, G. Topological type-II nodal line semimetal and Dirac semimetal state in stable kagome compound Mg₃Bi₂. *The journal of physical chemistry letters* **8**, 4814-4819 (2017).
- 190 Li, C. *et al.* Rules for phase shifts of quantum oscillations in topological nodal-line semimetals. *Physical review letters* **120**, 146602 (2018).
- 191 Schoop, L. M. *et al.* Dirac cone protected by non-symmorphic symmetry and three-dimensional Dirac line node in ZrSiS. *Nature communications* **7**, 11696 (2016).
- 192 Huang, H., Jin, K.-H. & Liu, F. Topological nodal-line semimetal in nonsymmorphic Cmce-phase Ag₂S. *Physical Review B* **96**, 115106 (2017).
- 193 Wang, J. Antiferromagnetic topological nodal line semimetals. *Physical Review B* **96**, 081107 (2017).
- 194 Gao, L. *et al.* Epitaxial Growth of Honeycomb Monolayer CuSe with Dirac Nodal Line Fermions. *Advanced Materials* **30**, 1707055 (2018).
- 195 Sun, J.-P., Zhang, D. & Chang, K. Coexistence of topological nodal lines, Weyl points, and triply degenerate points in TaS. *Physical Review B* **96**, 045121 (2017).
- 196 Behrends, J., Rhim, J.-W., Liu, S., Grushin, A. G. & Bardarson, J. H. Nodal-line semimetals from Weyl superlattices. *Physical Review B* **96**, 245101 (2017).
- 197 Wang, X.-B. *et al.* Topological surface electronic states in candidate nodal-line semimetal CaAgAs. *Physical Review B* **96**, 161112 (2017).
- 198 Kawakami, T. & Hu, X. Symmetry-guaranteed nodal-line semimetals in an fcc lattice. *Physical Review B* **96**, 235307 (2017).
- 199 Niu, C. *et al.* Two-dimensional topological nodal line semimetal in layered X₂Y (X= Ca, Sr, and Ba; Y= As, Sb, and Bi). *Physical Review B* **95**, 235138 (2017).
- 200 Chen, H. *et al.* Prediction of two-dimensional nodal-line semimetals in a carbon nitride covalent network. *Journal of Materials Chemistry A* **6**, 11252-11259 (2018).
- 201 Quan, Y., Yin, Z. & Pickett, W. Single Nodal Loop of Accidental Degeneracies in Minimal Symmetry: Triclinic CaAs₃. *Physical review letters* **118**, 176402 (2017).
- 202 Yan, Z. *et al.* Nodal-link semimetals. *Physical Review B* **96**, 041103 (2017).
- 203 Chen, C. *et al.* Weyl-loop half-metal in Li₃(FeO₃)₂. *Physical Review B* **99**, 075131 (2019).
- 204 Xiao, M., Sun, X.-Q. & Fan, S. Nodal chain semimetal in geometrically frustrated systems. *Physical Review B* **99**, 094206 (2019).
- 205 Huang, H., Jiang, W., Jin, K.-H. & Liu, F. Tunable topological semimetal states with ultraflat nodal rings in strained YN. *Physical Review B* **98**, 045131 (2018).
- 206 Shao, D.-F., Zhang, S.-H., Dang, X. & Tsymbal, E. Y. Tunable two-dimensional Dirac nodal nets. *Physical Review B* **98**, 161104 (2018).

-
- 207 Gavrilenko, V., Perov, A., Protogenov, A., Turkevich, R. & Chulkov, E. V. Chain of Dirac spectrum loops of nodes in crossed magnetic and electric fields. *Physical Review B* **97**, 115204 (2018).
- 208 Bzdušek, T., Wu, Q., Rüegg, A., Sigrist, M. & Soluyanov, A. A. Nodal-chain metals. *Nature* **538**, 75 (2016).
- 209 Zhou, Y., Xiong, F., Wan, X. & An, J. Hopf-link topological nodal-loop semimetals. *Physical Review B* **97**, 155140 (2018).
- 210 Chang, P.-Y. & Yee, C.-H. Weyl-link semimetals. *Physical Review B* **96**, 081114 (2017).
- 211 Chen, W., Lu, H.-Z. & Hou, J.-M. Topological semimetals with a double-helix nodal link. *Physical Review B* **96**, 041102 (2017).
- 212 Bi, R., Yan, Z., Lu, L. & Wang, Z. Nodal-knot semimetals. *Physical Review B* **96**, 201305 (2017).
- 213 Gong, C., Xie, Y., Chen, Y., Kim, H.-S. & Vanderbilt, D. Symmorphic intersecting nodal rings in semiconducting layers. *Physical review letters* **120**, 106403 (2018).
- 214 Wang, S.-S., Liu, Y., Yu, Z.-M., Sheng, X.-L. & Yang, S. A. Hourglass Dirac chain metal in rhenium dioxide. *Nature communications* **8**, 1844 (2017).
- 215 Feng, X., Yue, C., Song, Z., Wu, Q. & Wen, B. Topological Dirac nodal-net fermions in A1B 2-type TiB 2 and ZrB 2. *Physical Review Materials* **2**, 014202 (2018).
- 216 Yu, W. C. *et al.* Nonsymmorphic cubic Dirac point and crossed nodal rings across the ferroelectric phase transition in LiOsO 3. *Physical Review Materials* **2**, 051201 (2018).
- 217 Lian, J. *et al.* Multi-loop node line states in ternary MgSrSi-type crystals. *npj Computational Materials* **5**, 10 (2019).
- 218 Cai, J., Xie, Y., Chang, P.-Y., Kim, H.-S. & Chen, Y.-P. Nodal-chain network, intersecting nodal rings and triple points coexisting in nonsymmorphic Ba3Si4. *Physical Chemistry Chemical Physics* (2018).
- 219 Fu, B.-B. *et al.* Dirac nodal surfaces and nodal lines in ZrSiS. *Science advances* **5**, eaau6459 (2019).
- 220 Liang, Q.-F., Zhou, J., Yu, R., Wang, Z. & Weng, H. Node-surface and node-line fermions from nonsymmorphic lattice symmetries. *Physical Review B* **93**, 085427 (2016).
- 221 Bzdušek, T. & Sigrist, M. Robust doubly charged nodal lines and nodal surfaces in centrosymmetric systems. *Physical Review B* **96**, 155105 (2017).
- 222 Wu, W. *et al.* Nodal surface semimetals: Theory and material realization. *Physical Review B* **97**, 115125 (2018).
- 223 Basov, D., Averitt, R. & Hsieh, D. Towards properties on demand in quantum materials. *Nature materials* **16**, 1077 (2017).
- 224 Schaffer, R., Lee, E. K.-H., Yang, B.-J. & Kim, Y. B. Recent progress on correlated electron systems with strong spin-orbit coupling. *Reports on Progress in Physics* **79**, 094504 (2016).
- 225 Abate, Y. *et al.* Recent progress on stability and passivation of black phosphorus. *Advanced Materials* **30**, 1704749 (2018).
- 226 Sheng, X.-L., Yu, Z.-M., Yu, R., Weng, H. & Yang, S. A. d orbital topological insulator and semimetal in the antiferroite Cu2S family: Contrasting spin Helicities, nodal box, and hybrid surface states. *The journal of physical chemistry letters* **8**, 3506-3511 (2017).
- 227 Zhang, X., Jin, L., Dai, X. & Liu, G. Highly anisotropic type-II nodal line state in pure titanium metal. *Applied Physics Letters* **112**, 122403 (2018).

-
- 228 Yu, R., Weng, H., Fang, Z., Dai, X. & Hu, X. Topological node-line semimetal and Dirac semimetal state in antiperovskite Cu₃PdN. *Physical review letters* **115**, 036807 (2015).
- 229 Chan, Y.-H., Chiu, C.-K., Chou, M. & Schnyder, A. P. Ca₃P₂ and other topological semimetals with line nodes and drumhead surface states. *Physical Review B* **93**, 205132 (2016).
- 230 Son, D. & Spivak, B. Chiral anomaly and classical negative magnetoresistance of Weyl metals. *Physical Review B* **88**, 104412 (2013).
- 231 Xiong, J. *et al.* Evidence for the chiral anomaly in the Dirac semimetal Na₃Bi. *Science* **350**, 413-416 (2015).
- 232 Li, J. *et al.* Topological quantum catalyst: Dirac nodal line states and a potential electrocatalyst of hydrogen evolution in the TiSi family. *Science China Materials* **61**, 23-29 (2018).
- 233 Rajamathi, C. R. *et al.* Weyl semimetals as hydrogen evolution catalysts. *Advanced Materials* **29**, 1606202 (2017).
- 234 Lee, S. R., Sharma, P. A., Lima-Sharma, A. L., Pan, W. & Nenoff, T. M. Topological quantum materials for realizing Majorana quasiparticles. *Chemistry of Materials* **31**, 26-51 (2018).
- 235 Zhang, C. *et al.* Quantum Hall effect based on Weyl orbits in Cd₃As₂. *Nature* **565**, 331 (2019).
- 236 Kong, D. *et al.* Ambipolar field effect in the ternary topological insulator (Bi_xSb_{1-x})₂Te₃ by composition tuning. *Nature nanotechnology* **6**, 705 (2011).
- 237 He, Q. L. *et al.* Tailoring exchange couplings in magnetic topological-insulator/antiferromagnet heterostructures. *Nature materials* **16**, 94 (2017).
- 238 Pesin, D. & MacDonald, A. H. Spintronics and pseudospintronics in graphene and topological insulators. *Nature materials* **11**, 409 (2012).
- 239 Huang, H., Zhou, S. & Duan, W. Type-II Dirac fermions in the PtSe₂ class of transition metal dichalcogenides. *Physical Review B* **94**, 121117 (2016).
- 240 Xiao, R. *et al.* Manipulation of type-I and type-II Dirac points in PdTe₂ superconductor by external pressure. *Physical Review B* **96**, 075101 (2017).
- 241 Zhang, T.-T. *et al.* From type-II triply degenerate nodal points and three-band nodal rings to type-II Dirac points in centrosymmetric zirconium oxide. *The journal of physical chemistry letters* **8**, 5792-5797 (2017).
- 242 Park, C.-H., Yang, L., Son, Y.-W., Cohen, M. L. & Louie, S. G. New generation of massless Dirac fermions in graphene under external periodic potentials. *Physical review letters* **101**, 126804 (2008).
- 243 Nomura, K., Ryu, S., Koshino, M., Mudry, C. & Furusaki, A. Quantum Hall effect of massless Dirac fermions in a vanishing magnetic field. *Physical review letters* **100**, 246806 (2008).
- 244 Zhou, X., Fang, C., Tsai, W.-F. & Hu, J. Theory of quasiparticle scattering in a two-dimensional system of helical Dirac fermions: Surface band structure of a three-dimensional topological insulator. *Physical Review B* **80**, 245317 (2009).
- 245 Zhou, S. *et al.* First direct observation of Dirac fermions in graphite. *Nature physics* **2**, 595 (2006).
- 246 Peres, N., Neto, A. C. & Guinea, F. Dirac fermion confinement in graphene. *Physical Review B* **73**, 241403 (2006).
- 247 Lee, D.-H. Surface states of topological insulators: The Dirac fermion in curved two-dimensional spaces. *Physical review letters* **103**, 196804 (2009).
- 248 Li, G. & Andrei, E. Y. Observation of Landau levels of Dirac fermions in graphite. *Nature physics* **3**, 623 (2007).

-
- 249 Groth, C., Wimmer, M., Akhmerov, A., Tworzydło, J. & Beenakker, C. Theory of the topological Anderson insulator. *Physical review letters* **103**, 196805 (2009).
- 250 Pal, P. B. Dirac, majorana, and weyl fermions. *American Journal of Physics* **79**, 485-498 (2011).
- 251 Jia, S., Xu, S.-Y. & Hasan, M. Z. Weyl semimetals, Fermi arcs and chiral anomalies. *Nature materials* **15**, 1140 (2016).
- 252 Huang, S.-M. *et al.* New type of Weyl semimetal with quadratic double Weyl fermions. *Proceedings of the National Academy of Sciences* **113**, 1180-1185 (2016).
- 253 Chang, T.-R. *et al.* Prediction of an arc-tunable Weyl Fermion metallic state in $\text{Mo}_x\text{W}_{1-x}\text{Te}_2$. *Nature communications* **7**, 10639 (2016).
- 254 Sun, Y., Wu, S.-C., Ali, M. N., Felser, C. & Yan, B. Prediction of Weyl semimetal in orthorhombic MoTe_2 . *Physical Review B* **92**, 161107 (2015).
- 255 Zhang, C.-L. *et al.* Signatures of the Adler–Bell–Jackiw chiral anomaly in a Weyl fermion semimetal. *Nature communications* **7**, 10735 (2016).
- 256 Koepnick, K. *et al.* TaIrTe_4 : A ternary type-II Weyl semimetal. *Physical Review B* **93**, 201101 (2016).
- 257 Dai, X., Lu, H.-Z., Shen, S.-Q. & Yao, H. Detecting monopole charge in Weyl semimetals via quantum interference transport. *Physical Review B* **93**, 161110 (2016).
- 258 Jiang, J.-H. Tunable topological Weyl semimetal from simple-cubic lattices with staggered fluxes. *Physical Review A* **85**, 033640 (2012).
- 259 Fulga, I. & Stern, A. Triple point fermions in a minimal symmorphic model. *Physical Review B* **95**, 241116 (2017).
- 260 Furusaki, A. Weyl points and Dirac lines protected by multiple screw rotations. *Science Bulletin* **62**, 788-794 (2017).
- 261 Pshenay-Severin, D., Ivanov, Y. V., Burkov, A. & Burkov, A. Band structure and unconventional electronic topology of CoSi . *Journal of Physics: Condensed Matter* **30**, 135501 (2018).
- 262 Cano, J., Bradlyn, B. & Vergniory, M. Multifold nodal points in magnetic materials. *arXiv preprint arXiv:1904.12867* (2019).
- 263 Song, H., Huang, S.-J., Fu, L. & Hermele, M. Topological phases protected by point group symmetry. *Physical Review X* **7**, 011020 (2017).
- 264 Ramires, A. & Lado, J. L. Impurity-induced triple point fermions in twisted bilayer graphene. *Physical Review B* **99**, 245118 (2019).
- 265 Hu, H., Hou, J., Zhang, F. & Zhang, C. Topological Triply Degenerate Points Induced by Spin-Tensor-Momentum Couplings. *Physical review letters* **120**, 240401 (2018).
- 266 Gao, W. *et al.* A possible candidate for triply degenerate point fermions in trigonal layered PtBi_2 . *Nature communications* **9** (2018).
- 267 Owerre, S. Magnonic triply-degenerate nodal points. *EPL (Europhysics Letters)* **120**, 57002 (2018).
- 268 Wang, J.-R., Liu, G.-Z. & Zhang, C.-J. Topological quantum critical point in a triple-Weyl semimetal: Non-Fermi-liquid behavior and instabilities. *Physical Review B* **99**, 195119 (2019).
- 269 Cheung, C.-H. *et al.* Systematic analysis for triple points in all magnetic symmorphic systems and symmetry-allowed coexistence of Dirac points and triple points. *New Journal of Physics* **20**, 123002 (2018).

-
- 270 Takane, D. *et al.* Dirac-node arc in the topological line-node semimetal HfSiS. *Physical Review B* **94**, 121108 (2016).
- 271 Takane, D. *et al.* Observation of Dirac-like energy band and ring-torus Fermi surface associated with the nodal line in topological insulator CaAgAs. *npj Quantum Materials* **3**, 1 (2018).
- 272 Liu, Z., Wang, H., Wang, Z., Yang, J. & Liu, F. Pressure-induced organic topological nodal-line semimetal in the three-dimensional molecular crystal Pd (ddd) 2. *Physical Review B* **97**, 155138 (2018).
- 273 Salmankurt, B. & Duman, S. First-principles study of structural, mechanical, lattice dynamical and thermal properties of nodal-line semimetals ZrXY (X= Si, Ge; Y= S, Se). *Philosophical Magazine* **97**, 175-186 (2017).
- 274 Bian, G. *et al.* Drumhead surface states and topological nodal-line fermions in TlTaSe 2. *Physical Review B* **93**, 121113 (2016).
- 275 Yan, Z. & Wang, Z. Tunable Weyl points in periodically driven nodal line semimetals. *Physical review letters* **117**, 087402 (2016).
- 276 Feng, B. *et al.* Experimental realization of two-dimensional Dirac nodal line fermions in monolayer Cu₂Si. *Nature communications* **8**, 1007 (2017).
- 277 Liu, J. *et al.* Strain-induced nonsymmorphic symmetry breaking and removal of Dirac semimetallic nodal line in an orthoperovskite iridate. *Physical Review B* **93**, 085118 (2016).
- 278 Hosen, M. M. *et al.* Tunability of the topological nodal-line semimetal phase in ZrSi X-type materials (X= S, Se, Te). *Physical Review B* **95**, 161101 (2017).
- 279 Yu, R., Wu, Q., Fang, Z. & Weng, H. From nodal chain semimetal to Weyl semimetal in HfC. *Physical review letters* **119**, 036401 (2017).
- 280 Molina, R. A. & González, J. Surface and 3D quantum Hall effects from engineering of exceptional points in nodal-line semimetals. *Physical review letters* **120**, 146601 (2018).
- 281 Xie, L. S. *et al.* A new form of Ca₃P₂ with a ring of Dirac nodes. *Apl Materials* **3**, 083602 (2015).
- 282 Rhim, J.-W. & Kim, Y. B. Landau level quantization and almost flat modes in three-dimensional semimetals with nodal ring spectra. *Physical Review B* **92**, 045126 (2015).
- 283 Sun, Y., Zhang, Y., Liu, C.-X., Felser, C. & Yan, B. Dirac nodal lines and induced spin Hall effect in metallic rutile oxides. *Physical Review B* **95**, 235104 (2017).
- 284 Nandkishore, R. Weyl and Dirac loop superconductors. *Physical Review B* **93**, 020506 (2016).
- 285 Kim, H.-S., Chen, Y. & Kee, H.-Y. Surface states of perovskite iridates AIrO₃: signatures of a topological crystalline metal with nontrivial Z₂ index. *Physical Review B* **91**, 235103 (2015).
- 286 Chen, Y., Kim, H.-S. & Kee, H.-Y. Topological crystalline semimetals in nonsymmorphic lattices. *Physical Review B* **93**, 155140 (2016).
- 287 González, J. & Molina, R. Topological protection from exceptional points in Weyl and nodal-line semimetals. *Physical Review B* **96**, 045437 (2017).
- 288 Hosur, P., Dai, X., Fang, Z. & Qi, X.-L. Time-reversal-invariant topological superconductivity in doped Weyl semimetals. *Physical Review B* **90**, 045130 (2014).
- 289 Sun, K., Liu, W. V., Hemmerich, A. & Sarma, S. D. Topological semimetal in a fermionic optical lattice. *Nature Physics* **8**, 67 (2012).
- 290 Chiu, C.-K. & Schnyder, A. P. Classification of reflection-symmetry-protected topological semimetals and nodal superconductors. *Physical Review B* **90**, 205136 (2014).

-
- 291 Ahn, J., Kim, D., Kim, Y. & Yang, B.-J. Band Topology and Linking Structure of Nodal Line Semimetals with Z_2 Monopole Charges. *Physical review letters* **121**, 106403 (2018).
- 292 Fletcher, J. *et al.* Evidence for a nodal-line superconducting state in LaFePO. *Physical Review Letters* **102**, 147001 (2009).
- 293 Krüger, F. & Zaanen, J. Fermionic quantum criticality and the fractal nodal surface. *Physical Review B* **78**, 035104 (2008).
- 294 Takahashi, R., Hirayama, M. & Murakami, S. Spinless hourglass nodal-line semimetals. *Physical Review B* **96**, 155206 (2017).
- 295 Rauch, T., Minh, H. N., Henk, J. & Mertig, I. Model for ferromagnetic Weyl and nodal line semimetals: Topological invariants, surface states, anomalous and spin Hall effect. *Physical Review B* **96**, 235103 (2017).
- 296 Chen, C. *et al.* Dirac line nodes and effect of spin-orbit coupling in the nonsymmorphic critical semimetals M SiS (M= Hf, Zr). *Physical Review B* **95**, 125126 (2017).
- 297 Sun, J.-P. Topological Nodal Line Semimetal in Non-Centrosymmetric PbTaS. *Chinese Physics Letters* **34**, 077101 (2017).
- 298 Wang, R. *et al.* Nodal line fermions in magnetic oxides. *Physical Review B* **97**, 241111 (2018).
- 299 Shapourian, H., Wang, Y. & Ryu, S. Topological crystalline superconductivity and second-order topological superconductivity in nodal-loop materials. *Physical Review B* **97**, 094508 (2018).
- 300 Yu, J. Measuring Hopf links and Hopf invariants in a quenched topological Raman lattice. *Physical Review A* **99**, 043619 (2019).
- 301 Ezawa, M. Topological semimetals carrying arbitrary Hopf numbers: Fermi surface topologies of a Hopf link, Solomon's knot, trefoil knot, and other linked nodal varieties. *Physical Review B* **96**, 041202 (2017).
- 302 Tan, X. *et al.* Demonstration of Hopf-link semimetal bands with superconducting circuits. *Applied Physics Letters* **112**, 172601 (2018).
- 303 Kobayashi, S. *et al.* Crossing-line-node semimetals: General theory and application to rare-earth trihydrides. *Physical Review B* **95**, 245208 (2017).
- 304 Lee, C. H. *et al.* Imaging nodal knots in momentum space through topoelectrical circuits. *arXiv preprint arXiv:1904.10183* (2019).
- 305 Sun, X.-Q., Zhang, S.-C. & Bzdušek, T. Conversion rules for Weyl points and nodal lines in topological media. *Physical review letters* **121**, 106402 (2018).
- 306 Zhou, Y., Xiong, F., Wan, X. & An, J. Hopf-link multi-Weyl-loop topological semimetals. *arXiv preprint arXiv:1801.04169* (2018).
- 307 Zhang, X., Jin, L., Dai, X., Chen, G. & Liu, G. Ideal inner nodal chain semimetals in Li₂XY (X= Ca, Ba; Y= Si, Ge) materials. *The journal of physical chemistry letters* **9**, 5358-5363 (2018).
- 308 Wang, J. *et al.* Pseudo Dirac nodal sphere semimetal. *Physical Review B* **98**, 201112 (2018).
- 309 Loos, P.-F. & Bressanini, D. Nodal surfaces and interdimensional degeneracies. *The Journal of chemical physics* **142**, 214112 (2015).
- 310 Brzezicki, W., Cuoco, M., Forte, F. & Oleś, A. M. Topological phases emerging from spin-orbital physics. *Journal of Superconductivity and Novel Magnetism* **31**, 639-645 (2018).
- 311 Zhang, L. *et al.* Structural and electronic properties of germanene on MoS₂. *Physical review letters* **116**, 256804 (2016).

-
- 312 Grimme, S., Brandenburg, J. G., Bannwarth, C. & Hansen, A. Consistent structures and interactions by density functional theory with small atomic orbital basis sets. *The Journal of chemical physics* **143**, 054107 (2015).
- 313 Ridolfi, E., Le, D., Rahman, T., Mucciolo, E. & Lewenkopf, C. A tight-binding model for MoS₂ monolayers. *Journal of Physics: Condensed Matter* **27**, 365501 (2015).
- 314 Liu, M.-H. *et al.* Scalable tight-binding model for graphene. *Physical review letters* **114**, 036601 (2015).
- 315 Zhu, Q., Oganov, A. R., Salvadó, M. A., Pertierra, P. & Lyakhov, A. O. Denser than diamond: ab initio search for superdense carbon allotropes. *Physical Review B* **83**, 193410 (2011).
- 316 Yang, L., Park, C.-H., Son, Y.-W., Cohen, M. L. & Louie, S. G. Quasiparticle energies and band gaps in graphene nanoribbons. *Physical Review Letters* **99**, 186801 (2007).
- 317 Khomyakov, P. *et al.* First-principles study of the interaction and charge transfer between graphene and metals. *Physical Review B* **79**, 195425 (2009).
- 318 Ortix, C., Yang, L. & van den Brink, J. Graphene on incommensurate substrates: trigonal warping and emerging Dirac cone replicas with halved group velocity. *Physical Review B* **86**, 081405 (2012).
- 319 Jiang, X., Zhao, J., Li, Y. L. & Ahuja, R. Tunable Assembly of sp³ Cross - Linked 3D Graphene Monoliths: A First - Principles Prediction. *Advanced Functional Materials* **23**, 5846-5853 (2013).
- 320 Hu, J. *et al.* Three-dimensional honeycomb carbon: Junction line distortion and novel emergent fermions. *Carbon* **141**, 417-426 (2019).
- 321 Chen, Y. *et al.* Nexus networks in carbon honeycombs. *Physical Review Materials* **2**, 044205 (2018).
- 322 Greilich, A. *et al.* Optical control of spin coherence in singly charged (In, Ga) As/GaAs quantum dots. *Physical review letters* **96**, 227401 (2006).
- 323 Cragg, D. M., Sherrington, D. & Gabay, M. Instabilities of an m-Vector Spin-Glass in a Field. *Physical Review Letters* **49**, 158 (1982).
- 324 Kan, M. *et al.* Tuning magnetic properties of graphene nanoribbons with topological line defects: From antiferromagnetic to ferromagnetic. *Physical Review B* **85**, 155450 (2012).
- 325 Ruffieux, P. *et al.* On-surface synthesis of graphene nanoribbons with zigzag edge topology. *Nature* **531**, 489 (2016).
- 326 Güçlü, A. D., Grabowski, M. & Hawrylak, P. Electron-electron interactions and topology in the electronic properties of gated graphene nanoribbon rings in Möbius and cylindrical configurations. *Physical Review B* **87**, 035435 (2013).
- 327 Gröning, O. *et al.* Engineering of robust topological quantum phases in graphene nanoribbons. *Nature* **560**, 209 (2018).
- 328 Rizzo, D. J. *et al.* Topological band engineering of graphene nanoribbons. *Nature* **560**, 204 (2018).
- 329 Cao, T., Zhao, F. & Louie, S. G. Topological phases in graphene nanoribbons: junction states, spin centers, and quantum spin chains. *Physical review letters* **119**, 076401 (2017).
- 330 Yao, Y., Ye, F., Qi, X.-L., Zhang, S.-C. & Fang, Z. Spin-orbit gap of graphene: First-principles calculations. *Physical Review B* **75**, 041401 (2007).
- 331 Gomes, K. K., Mar, W., Ko, W., Guinea, F. & Manoharan, H. C. Designer Dirac fermions and topological phases in molecular graphene. *Nature* **483**, 306 (2012).
- 332 Sigrist, M. & Rice, T. Paramagnetic effect in high T_c superconductors—a hint for d-wave

-
- superconductivity. *Journal of the Physical Society of Japan* **61**, 4283-4286 (1992).
- 333 Monthoux, P., Balatsky, A. & Pines, D. Toward a theory of high-temperature superconductivity in the antiferromagnetically correlated cuprate oxides. *Physical review letters* **67**, 3448 (1991).
- 334 Kitaev, A. in *AIP Conference Proceedings*. 22-30 (AIP).
- 335 Gao, Y. *et al.* A class of topological nodal rings and its realization in carbon networks. *Physical Review B* **97**, 121108 (2018).
- 336 Zyuzin, A. A. & Zyuzin, A. Y. Flat band in disorder-driven non-Hermitian Weyl semimetals. *Physical Review B* **97**, 041203 (2018).
- 337 Yin, H. *et al.* Stone-Wales graphene: A two-dimensional carbon semimetal with magic stability. *Physical Review B* **99**, 041405 (2019).
- 338 Kim, B. G. & Choi, H. J. Graphyne: Hexagonal network of carbon with versatile Dirac cones. *Physical Review B* **86**, 115435 (2012).
- 339 Gülseren, O., Yildirim, T., Ciraci, S. & Kılıç, Ç. Reversible band-gap engineering in carbon nanotubes by radial deformation. *Phys. Rev. B* **65**, 155410, doi:10.1103/PhysRevB.65.155410 (2002).
- 340 Schnyder, A. P., Ryu, S., Furusaki, A. & Ludwig, A. W. Classification of topological insulators and superconductors in three spatial dimensions. *Physical Review B* **78**, 195125 (2008).
- 341 Matsuura, S., Chang, P.-Y., Schnyder, A. P. & Ryu, S. Protected boundary states in gapless topological phases. *New Journal of Physics* **15**, 065001 (2013).
- 342 Teo, J. C. & Kane, C. L. Topological defects and gapless modes in insulators and superconductors. *Physical Review B* **82**, 115120 (2010).
- 343 Zhong, C. *et al.* Three-dimensional Pentagon Carbon with a genesis of emergent fermions. *Nature communications* **8**, 15641 (2017).
- 344 Georgi, H. *Lie algebras in particle physics: from isospin to unified theories*. (CRC Press, 2018).
- 345 Charlier, J.-C., Michenaud, J.-P. & Gonze, X. First-principles study of the electronic properties of simple hexagonal graphite. *Physical Review B* **46**, 4531 (1992).
- 346 Fidkowski, L. & Kitaev, A. Effects of interactions on the topological classification of free fermion systems. *Physical Review B* **81**, 134509 (2010).
- 347 Gao, Y., Xie, Y., Chen, Y., Gu, J. & Chen, Z. Spindle nodal chain in three-dimensional α' boron. *Physical Chemistry Chemical Physics* **20**, 23500-23506 (2018).
- 348 Zhang, H. *et al.* Dirac nodal lines and tilted semi-Dirac cones coexisting in a striped boron sheet. *The journal of physical chemistry letters* **8**, 1707-1713 (2017).
- 349 Gupta, S., Kutana, A. & Yakobson, B. I. Dirac Cones and Nodal Line in Borophene. *The journal of physical chemistry letters* **9**, 2757-2762 (2018).
- 350 Feng, B. *et al.* Dirac fermions in borophene. *Physical review letters* **118**, 096401 (2017).
- 351 Ma, F. *et al.* Graphene-like two-dimensional ionic boron with double dirac cones at ambient condition. *Nano letters* **16**, 3022-3028 (2016).
- 352 Zhou, X.-F. *et al.* Semimetallic two-dimensional boron allotrope with massless Dirac fermions. *Physical Review Letters* **112**, 085502 (2014).
- 353 Heikkilä, T. T. & Volovik, G. E. Nexus and Dirac lines in topological materials. *New Journal of Physics* **17**, 093019 (2015).
- 354 Rajca, A., Safronov, A., Rajca, S., Schoemaker, R. Double helical octaphenylene. *Angew. Chem. Int. Ed.* **36**, 488 (1997).

-
- 355 Rajca, A. Wang, H. Bolshov, P. Rajca, S. Greek cross dodecaphenylene: sparteine-mediated asymmetric synthesis of chiral D₂-symmetric π -conjugated tetra-o-phenylenes. *Tetrahedron* **57**, 3725 (2001).
- 356 Xu, C. & Balents, L. Topological superconductivity in twisted multilayer graphene. *Physical review letters* **121**, 087001 (2018).
- 357 Cao, Y. *et al.* Correlated insulator behaviour at half-filling in magic-angle graphene superlattices. *Nature* **556**, 80 (2018).
- 358 Cao, Y. *et al.* Unconventional superconductivity in magic-angle graphene superlattices. *Nature* **556**, 43 (2018).
- 359 Chebrolov, N. R., Chittari, B. L. & Jung, J. Flatbands in twisted bi-bilayer graphene. *arXiv preprint arXiv:1901.08420* (2019).
- 360 Jorio, A. & Cançado, L. G. Raman spectroscopy of twisted bilayer graphene. *Solid State Communications* **175**, 3-12 (2013).
- 361 Guinea, F. & Walet, N. R. Electrostatic effects, band distortions, and superconductivity in twisted graphene bilayers. *Proceedings of the National Academy of Sciences* **115**, 13174-13179 (2018).
- 362 Yin, L.-J. *et al.* Landau quantization and Fermi velocity renormalization in twisted graphene bilayers. *Physical Review B* **92**, 201408 (2015).
- 363 Isobe, H., Yuan, N. F. & Fu, L. Unconventional superconductivity and density waves in twisted bilayer graphene. *Physical Review X* **8**, 041041 (2018).
- 364 Thomson, A., Chatterjee, S., Sachdev, S. & Scheurer, M. S. Triangular antiferromagnetism on the honeycomb lattice of twisted bilayer graphene. *Physical Review B* **98**, 075109 (2018).
- 365 Koshino, M. *et al.* Maximally localized Wannier orbitals and the extended Hubbard model for twisted bilayer graphene. *Physical Review X* **8**, 031087 (2018).
- 366 Kim, K. *et al.* Tunable moiré bands and strong correlations in small-twist-angle bilayer graphene. *Proceedings of the National Academy of Sciences* **114**, 3364-3369 (2017).
- 367 Morell, E. S., Correa, J., Vargas, P., Pacheco, M. & Barticevic, Z. Flat bands in slightly twisted bilayer graphene: Tight-binding calculations. *Physical Review B* **82**, 121407 (2010).
- 368 Liu, Z. *et al.*, Realization of flat band with possible nontrivial topology in electronic Kagome lattice. *Sci. Adv.* **4**, eaau4511 (2018).